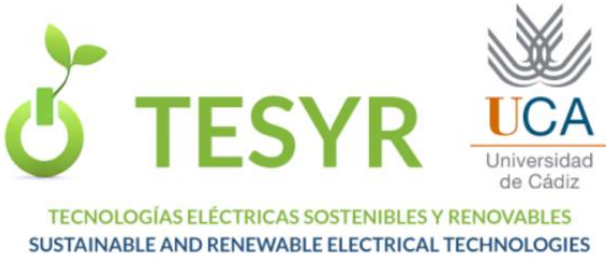

Universidad de Cádiz

Optimal Control Strategy Based on Differential Evolution Algorithm for Seamless Transition Between Islanded and Grid-Connected Operation Modes in Microgrid Clusters

Horrillo Quintero, Pablo; García Triviño, Pablo; Carrasco González, David; Fernández Ramírez, Luis Miguel

Published in:
Expert Systems with Application

DOI (link to publication from Publisher):
10.1016/J.ESWA.2025.129461

Publication date:
2026

Document Version:
Accepted

Citation for published version (IEEE):
P. Horrillo-Quintero, P. García-Triviño, D. Carrasco-González, and L. M. Fernández-Ramírez, "Optimal control strategy based on differential evolution algorithm for seamless transition between islanded and grid-connected operation modes in microgrid clusters," Expert Syst Appl, vol. 297, p. 129461, Feb. 2026, doi: 10.1016/J.ESWA.2025.129461.

Expert Systems With Applications 297 (2026) 129461

Contents lists available at ScienceDirect

Expert Systems With Applications

journal homepage: www.elsevier.com/locate/eswa

Optimal control strategy based on differential evolution algorithm for seamless transition between islanded and grid-connected operation modes in microgrid clusters

Pablo Horrillo-Quintero, Pablo García-Triviño, David Carrasco-González, Luis M. Fernández-Ramírez *

Research Group in Sustainable and Renewable Electrical Technologies (PAIDI-TEP023), Department of Electrical Engineering, Higher Technical School of Engineering of Algeciras (ETSIA), University of Cádiz, Avda. Ramón Puyol, s/n, 11202 Algeciras, Cádiz, Spain

ARTICLE INFO

Keywords:
Microgrid cluster
Seamless synchronization
Grid-forming inverter
Grid-feeding inverter
Differential evolution

ABSTRACT

The increasing integration of renewable energy sources and distributed energy resources is accelerating the transformation of traditional power systems into smart grids. This transformation relies heavily on the deployment of microgrids (MGs), which offer enhanced flexibility, resilience, and sustainability. However, ensuring the stable and efficient synchronization of MGs, especially during transitions between islanded and grid-connected modes, remains a critical and unresolved challenge. This challenge is further amplified in MG clusters (MGCs), where coordinated operation is essential to maintain power quality and system reliability. Driven by the need to address this challenge, this study proposes a real-time synchronization control method to enhance the dynamic performance and operational reliability of MGCs. The main objective is to design and validate an optimal control strategy capable of minimizing frequency deviations and improving power sharing during the synchronization process. To achieve this, an optimal seamless synchronization control based on a differential evolution (DE) algorithm is developed. This controller optimizes a frequency error control objective function in real time and is tested on an MGC architecture combining grid-forming (GFM) and grid-feeding (GFD) inverters. This work addresses the lack of robust, fast, and quantifiable synchronization methods for hybrid inverter-based MGCs, a gap that this study aims to fill. The proposed method enables accurate optimization of the transition between islanded and grid-connected modes. Simulation results demonstrate substantial performance gains: a 66.33% reduction in the ITSE compared to a synchronization strategy based on the fmincon optimization algorithm, and a 37.91% improvement over a conventional approach that adjusts synchronization by modifying the droop control coefficients. Furthermore, a comparative analysis with the particle swarm optimization (PSO) algorithm demonstrated that the DE-based approach reduces computation time by 20.29%, highlighting its superior efficiency and suitability for real-time embedded implementation. A sensitivity analysis involving 500 different scenarios, including evaluations under fault conditions, confirms the robustness of the approach. The average ITSE for these 500 simulations was 0.2459, with a standard deviation of 0.041, demonstrating consistent and reliable performance under varying load conditions. Moreover, a second sensitivity analysis, conducted over 250 simulations, identified the optimal DE parameters, enabling the selection of an effective combination of population size, mutation factor, and crossover rate. Finally, experimental validation using a Hardware-in-the-Loop setup, with an OPAL-RT4512 unit and a dSPACE MicroLabBox, verifies the effectiveness and real-time performance of the proposed control strategy.

1. Introduction

Microgrids (MGs) are essential in smart grids due to the possibility that they offer of combining local distributed energy resources (DERs) and loads within distribution networks. Moreover, it is possible to connect several nearby MGs to build a microgrid cluster (MGC), thereby

* Corresponding author.
E-mail addresses: pablo.horrillo@uca.es (P. Horrillo-Quintero), pablo.garcia@uca.es (P. García-Triviño), david.carrasco@uca.es (D. Carrasco-González), luis.fernandez@uca.es (L.M. Fernández-Ramírez).

https://doi.org/10.1016/j.eswa.2025.129461
Received 27 May 2025; Received in revised form 24 July 2025; Accepted 20 August 2025
Available online 27 August 2025

enhancing flexibility, resilience and operational efficiency (Jin et al., 2024). This arrangement enables MGs to handle operations independently when operate in grid-connected (GC) mode, promoting cost-efficient functioning (Gabbar and Abdelsalam, 2014). Furthermore, MGCs can operate independently, relying on DERs and energy storage systems (ESSs) to act as self-sufficient energy sources, which bolsters reliability, robustness, and security (Tang et al., 2025). The capability to alternate between GC and islanded (IS) modes grants modern active distribution grids centered on MGs greater flexibility compared to traditional power systems characterized by one-way power flow. Therefore, proper coordination with the distribution network operator remains essential.

The main role of GC-MGCs is to generate a specified controlled amount of power (Liu et al., 2024), aiming to achieve an optimal energy distribution considering costs, losses, or emissions. However, these systems do not manage frequency and voltage regulation. In contrast, MGCs operating in IS mode are primarily responsible for regulating frequency and voltage (Hmad et al., 2023). One of the key challenges in current research is achieving smooth synchronization of MGCs with the main grid, largely due to the widespread use of low inertia MGs based on DERs and ESSs in both GC and IS modes (Yi et al., 2022); (Koohi-Kamali and Rahim, 2016).

According to (D'Silva et al., 2020); (Rezaei and Kalantar, 2015), the main issues associated with the seamless transition between GC and IS modes are as follows: 1) frequency variations that cause disruptions in the stability of the MGC, and 2) significant fluctuations in the voltage and current output of the linking converter due to changes in its operating mode.

Droop control-based strategies are among the most widely implemented approaches that enable a smooth transition (Ghosh and Zare, 2023). Authors in (Ganjian-Aboukheili et al., 2020) proposed an adapted droop control coefficients to replicate the inertia characteristics of a synchronous generator from GC to IS mode. However, the performance of the transition algorithm between both modes was not evaluated quantitatively. In (Hennane et al., 2022), a distributed nonlinear control strategy based on droop control was proposed to enhance the synchronization and power sharing of distributed generators (DGs) in a mesh MG under both islanded and grid-connected modes. The approach enabled seamless transitions between modes without compromising the balance of active and reactive power. While this work provided a robust synchronization framework for individual DGs, its scope remains limited to local control schemes without addressing global optimal coordination across MGCs. A modification of the droop control technique was employed in (Shahab and Wang, 2021), where the droop coefficients were replaced with transfer functions in a double control loop. Nevertheless, only time-domain results were presented, and the practical validation of the proposed approach was not demonstrated. The modified droop control technique was also implemented in (Cao et al., 2023), where a reverse droop control strategy was proposed to address the AC voltage and frequency imbalances during mode transitions. This approach enabled the output power of the linking converter to adjust dynamically to the rated load, reducing voltage and frequency deviations.

The adaptation of the virtual synchronous machine control strategy was proposed in (Huaman et al., 2024) to smooth grid reconnection transitions by synchronizing with the main grid. While this approach reduced voltage transients and minimized amplitude and frequency deviations compared to traditional control methods, the synchronization process itself was not optimized. Instead, it relied on conventional control layers without employing advanced optimization techniques to enhance reconnection dynamics and further reduce transient disturbances A pre-synchronization strategy for virtual synchronous generator converters was proposed in (Liu et al., 2024) to align the output voltage parameters—frequency, amplitude, and phase—with those of the main grid prior to reconnection. The approach relied on traditional phase locked loop (PLL) techniques combined with droop control. While the method allowed for a smooth adjustment of the VSG output to meet grid requirements, the use of conventional PI controllers limited the dynamic adaptability and optimal performance of the synchronization process, especially under fast-changing conditions. Similarly, (Gong et al., 2024), presented a tuning of PI controllers based on the golden jackal optimization algorithm to enhance synchronization performance. However, the underlying PI structure remained unchanged. As a result, the control may suffer from limited robustness in the presence of nonlinearities, rapid transients, or significant disturbances, especially under varying grid conditions.

Droop control technique, even with modifications, remains inherently slow due to the required temporal decoupling from voltage controllers in order to preserve system stability. To mitigate this drawback, advanced nonlinear control methods, such as virtual oscillator control (Awal et al., 2020), have been proposed. Additionally, the deployment of dispatchable units, particularly ESSs (Talapur et al., 2018), has been suggested to enhance system performance. In (Khan et al., 2023), a synchronization algorithm was developed to ensure the smooth reconnection of an islanded MG to the utility grid. The method introduced an adaptive control scheme to regulate transient behavior through a two-stage process composed of a synchronization loop and a set of stopping criteria. Nonetheless, the approach did not incorporate an optimization strategy for the synchronization process, which could have further improved the efficiency and performance of the transition. The work presented in (Li et al., 2024) developed a distributed cooperative synchronization strategy for multiple parallel grid-supporting inverters within an AC MGs. Each inverter relied on local measurements to estimate the grid phase angle and communicated with neighbouring units to collectively achieve synchronization. Nevertheless, although the approach effectively prevented single points of failure and enabled inverter coordination, the synchronization process was not optimized.

A generalized fourth-order filter was employed in (Yadav et al., 2024) to estimate the fundamental components and the phase angle for synchronization, with the aim of enhancing power quality and ensuring smooth switching. Although the system demonstrated good performance under certain test scenarios, it lacked dynamic coordination mechanisms capable of adapting to fast transients or highly variable conditions. Similarly, an optimal Kalman filter-based phase-locked loop was proposed in (Buduma et al., 2021) to accurately estimate the phase and frequency of the grid voltage signal during MG synchronization. The Kalman filter gains were optimized by tuning the covariance matrices using a particle swarm optimization algorithm. However, this method was not applied or validated for the synchronization of a MGC, limiting its direct applicability to more complex MGC scenarios.

Intelligent control algorithms have been also proposed for smooth transitions between IS and GC modes. In (Khan et al., 2023), fuzzy proportional-integral and steepest descent-based fuzzy logic (FL) controllers were employed to enhance synchronization and handle uncertainties, ensuring a seamless reconnection to the utility grid. Similarly, in (Hmad et al., 2019), a FL approach facilitated a smooth transition between GC and IS modes by enabling gradual mode shifting and enhancing disturbance rejection through optimized voltage loop control. However, a practical implementation was not demonstrated in these studies.

The model predictive control (MPC) technique has been used to facilitate a seamless transition to the main grid (Fachini et al., 2024). An enhanced adaptive MPC approach for grid-forming (GFM) converters was proposed in (Meng et al., 2023) to facilitate seamless transitions from islanded to grid-connected states. It focused on minimizing voltage, current, and frequency fluctuations during the transition, while optimizing frequency stability and response speed. Similarly, an MPC for a voltage source inverter was introduced in (Li et al., 2017), using a simple synchronization algorithm through the application of a second-order generalized integrator. However, MPC requires system linearization—a process that can be particularly challenging for MGCs due to their significant nonlinearities—and also demands precise tuning of

the weighting coefficients.

Although the synchronization of MGCs between IS and GC modes is a current area of research, the existing literature presents several limitations that have yet to be adequately addressed. In the majority of studies (Ganjian-Aboukheili et al., 2020; Shahab and Wang, 2021; Cao et al., 2023), the transition between these modes is managed through an approach that modifies the droop control coefficients, which results in slower system responses (D'Silva et al., 2020). Moreover, deviations in frequency and voltage become more significant (Poonahela et al., 2023), and the system shows increased sensitivity to disturbances (Xu et al., 2021). Most works address the synchronization issue from a qualitative perspective, lacking a numerical approach that would allow for a quantifiable assessment of the control effectiveness (Ganjian-Aboukheili et al., 2020), thus hindering the accurate evaluation of its performance. Another critical factor to consider is the practical viability of the proposed solutions. While fuzzy logic-based algorithms (Khan et al., 2023; Hmad et al., 2019) have demonstrated their effectiveness in time-domain simulations, their experimental validation remains unproven. Approaches based on MPC (Fachini et al., 2024; Meng et al., 2023; Li et al., 2017) require plant linearization and precise tuning, which can be a complex and challenging task.

In this context, the present work offers significant advancements over the existing literature by introducing a quantitatively validated and experimentally verified synchronization strategy that optimizes the transition between IS and GC modes in MGCs. Unlike conventional droop control methods that cause slow responses and instability during mode switching, the proposed approach applies a differential evolution (DE) algorithm to dynamically and optimally coordinate power sharing between GFM and grid-feeding (GFD) inverters. This enables faster, smoother, and more stable synchronization, effectively eliminating frequency fluctuations and voltage deviations typically observed in previous works. Furthermore, this study introduces a novel objective function based on integral time square error (ITSE) to rigorously quantify synchronization performance, providing a clear and consistent metric for optimization and comparison. The control strategy is also validated against IEEE Std. 1547–2018, ensuring compliance with industry standards. Importantly, the practical feasibility of the proposed method is demonstrated through comprehensive hardware-in-the-loop (HIL) testing, confirming its real-time implementation capabilities and robustness—an aspect often missing in previous research. Collectively, these contributions address key gaps in the literature and deliver a more reliable and effective synchronization framework suited to the increasing complexity of modern MGC.

Table 1 presents a comparative overview of seven key aspects addressed in this work, which have not been comprehensively covered in previous synchronization approaches. These aspects include the experimental validation ('Experimental Validation' in Table 1), the integration of an optimization algorithm within the synchronization framework ('Optimization Algorithm'), the use of a quantitative metric to assess synchronization performance ('Quantifies Synchronization'), the achievement of smooth synchronization between GC and IS modes ('Smooth GC-IS transition'), the implementation of an advanced control strategy ('Advanced Control Strategy'), the combined use of both GFM and GFD inverters ('Coordination of GFM & GFD'), and compliance with the IEEE 1547–2018 standard ('IEEE 1547'). First, this paper introduces a quantitatively optimized synchronization procedure, using the widely recognized ITSE as a performance metric. In addition to achieving a stable synchronization, the proposed method strictly complies with the IEEE 1547–2018 standard, thereby ensuring validation against a well-established international benchmark. Furthermore, the DE meta-heuristic optimization algorithm is employed, offering notable computational efficiency and ease of implementation for real-time applications. Another novel contribution lies in the design of the MGC architecture, which integrates both GFM and GFD inverters based on MGs. This hybrid configuration enhances the system's flexibility and robustness, yet remains largely unexplored in the existing literature. To the best of the authors' knowledge, no prior study has simultaneously addressed all these aspects within a unified control and synchronization framework.

The primary contributions of this work in response to the challenges previously discussed are outlined as follows:

1) Development and implementation of a novel synchronization control system that enables an optimal, seamless transition between IS and GC modes. This proposed approach integrates a DE algorithm to intelligently optimize the power setpoints of MGs linked with both GFM and GFD inverters. By coordinating these inverter types, the proposed method effectively mitigates frequency oscillations and voltage deviations during mode transitions, significantly improving dynamic response times compared to traditional droop control-based techniques and optimization techniques. This coordination mechanism enhances stability and robustness in real operating conditions, where rapid and precise synchronization is essential.

2) Introduction of a rigorous quantitative framework for evaluating synchronization performance, based on a newly formulated objective

Table 1
Comparison of Existing and Proposed Methods for Synchronization Between IS and GC Modes in MGCs.

Ref	ExperimentalValidation	OptimizationAlgorithm	Quantifies Synchronization (e.g ITSE)	Smooth GC-IS transition	Advanced ControlStrategy	Coordination of GFM & GFD	IEEE 1547
(Ganjian-Aboukheili et al., 2020)	✓	×	×	✓	✓	×	×
(Hennane et al., 2022)	✓	×	×	✓	✓	×	×
(Shahab and Wang, 2021)	✓	×	×	✓	✓	×	×
(Cao et al., 2023)	×	×	×	✓	×	×	×
(Huaman et al., 2024)	×	✓	×	✓	✓	×	×
(Liu et al., 2024)	×	×	×	✓	×	×	×
(Gong et al., 2024)	✓	×	×	✓	✓	×	×
(Awal et al., 2020)	✓	×	×	✓	✓	×	×
(Talapur et al., 2018)	✓	×	×	✓	×	×	×
(Khan et al., 2023)	×	×	×	✓	×	×	×
(Li et al., 2024)	✓	×	×	✓	×	×	✓
(Yadav et al., 2024)	✓	×	✓	✓	✓	×	✓
(Buduma et al., 2021)	✓	✓	×	✓	✓	×	×
(Khan et al., 2023)	×	✓	✓	✓	✓	×	✓
(Hmad et al., 2019)	×	✓	✓	✓	✓	×	✓
(Fachini et al., 2024)	×	✓	✓	✓	✓	×	✓
(Meng et al., 2023)	✓	✓	×	✓	✓	×	✓
(Li et al., 2017)	×	×	×	✓	×	×	✓
Paper	✓	✓	✓	✓	✓	✓	✓

function that minimizes ITSE of frequency deviations during synchronization events. The proposed DE algorithm enables systematic tuning and optimization of control parameters, providing a measurable metric for assessing control effectiveness. Additionally, the synchronization strategy is validated against the latest IEEE Std. 1547–2018 standards, ensuring compliance with industry requirements and supporting its applicability in real-world MG deployments.

3) Comprehensive experimental validation of the proposed synchronization strategy through hardware-in-the-loop (HIL) testing, using an OPAL-RT4512 real-time simulator and a dSPACE MicroLabBox controller. The control algorithm was initially tested through detailed time-domain simulations in MATLAB/Simulink, and subsequently implemented and verified under real-time conditions to demonstrate computational efficiency, robustness, and fidelity. This end-to-end validation confirms the practical feasibility of the proposed method and its readiness for deployment in real MG environments.

The rest of this paper is organized as follows: Section II presents the MGC under study. Section III introduces the synchronization control scheme that enables operation in both IS and GC modes. The DE algorithm proposed for optimizing the grid synchronization process is outlined in Section IV. Section V provides the results obtained and their discussion. Finally, Section VI presents the main conclusions drawn from this work.

2. Dynamic modelling of the MGC

To ensure stability in IS mode, at least one inverter must operate as GFM converter. This is essential for regulating voltage and frequency in the absence of a main grid. While droop control is the common approach to perform the power distribution, it does not provide direct control over active or reactive power based on predefined setpoints. Consequently, GFD inverters are thus employed to precisely control the power injection of MGs when required.

This paper presents an optimal combination of the two previously discussed inverter types for both operational modes. As depicted in Fig. 1, the proposed MGC consists of three MGs. Of these three MGs, two are coupled to GFM inverters, and the remaining one to a GFD inverter. The output voltage level is set at 480 V. Furthermore, to mitigate harmonic distortion and voltage fluctuations, an RLC filter is integrated. Next, an isolated transformer is utilized to step up the voltage level to 600 V. The MGs are interconnected via transmission lines to a point of common coupling (PCC). A circuit breaker facilitates the switching operation between the IS and GC modes.

In order to regulate the individual MG operation, a local control approach is employed for every inverter, utilizing a cascade structure. This methodology is commonly adopted in MG management due to its ability to enhance system control accuracy. By employing a nested-loop configuration, conventional linear control techniques can be effectively utilized, yielding improved response times and greater robustness against disturbances. In the studied MGC, there are four sequential controllers for the GFM inverters, while three controllers are dedicated to the GFD inverter. The cascade control architecture for the MGC is illustrated in Fig. 2.

The local control system for the MGs linked through GFM inverters includes a combination of a traditional droop control, current regulation, voltage management, and an inverter gate signal generator. The initial controller of this control scheme is the droop control, which defines the frequency of each MG according to the following equation:

$$f_i = f_{o,i} + n_i(P_{o,i} - P_i) \tag{1}$$

where the frequency for each MG is denoted as f_i, while $f_{o,i}$ represents the reference frequency. The droop control factor is labelled as n_i, and $P_{o,i}$ indicates the power corresponding to frequency $f_{o,i}$. Meanwhile, P_i represents the measured active power. Note that the subscript i pertains to each specific MG.

Adopting an analogous methodology, the output voltage of each MG (V_i) can be derived using the following equation:

$$V_i = V_{o,i} - m_i Q_i \tag{2}$$

In this context, the setpoint voltage is denoted as $V_{o,i}$, while m_i refers to the voltage droop control coefficient, and Q_i represents the reactive power. It is worth noting that, under the voltage droop control configuration, $Q_{o,i}$ is assumed to be zero.

The voltage control mechanism adjusts the values of the direct (V_d) and quadrature (V_q) voltage to match the reference target obtained from Eq. (2). To reduce the difference between the measured and setpoint values, a PI controller is adopted. This controller generates the necessary reference current values, which are expressed as I_d^*, I_q^*.

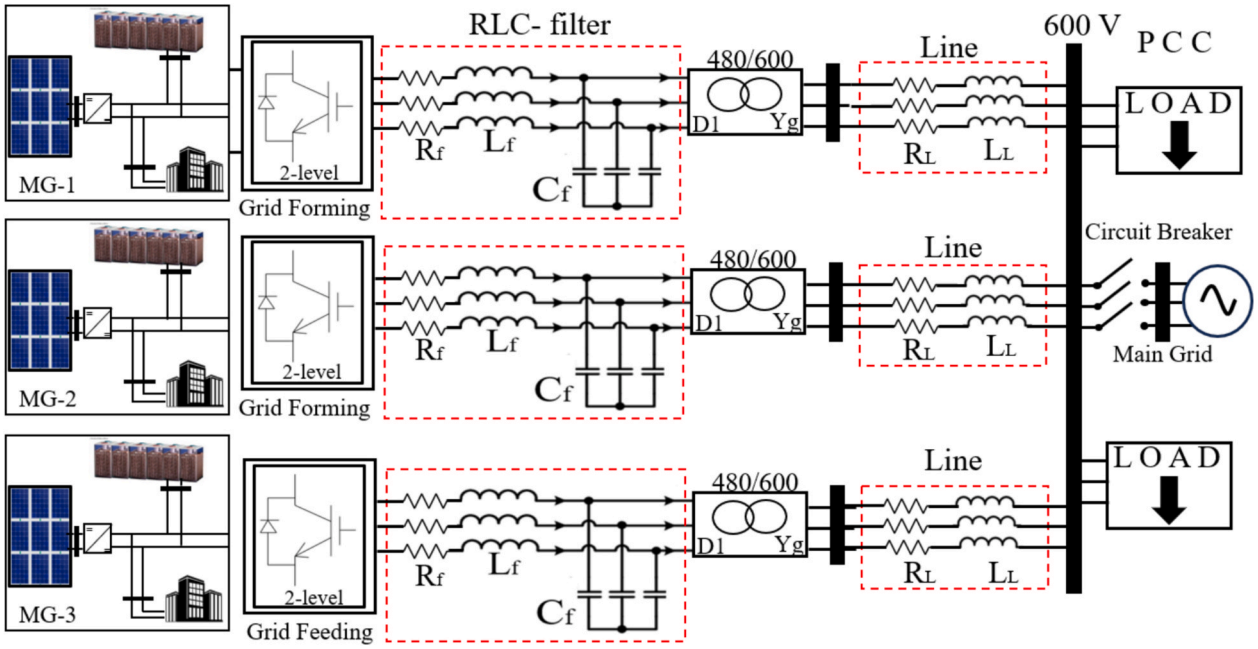

Fig. 1. Configuration of the MGC under study.

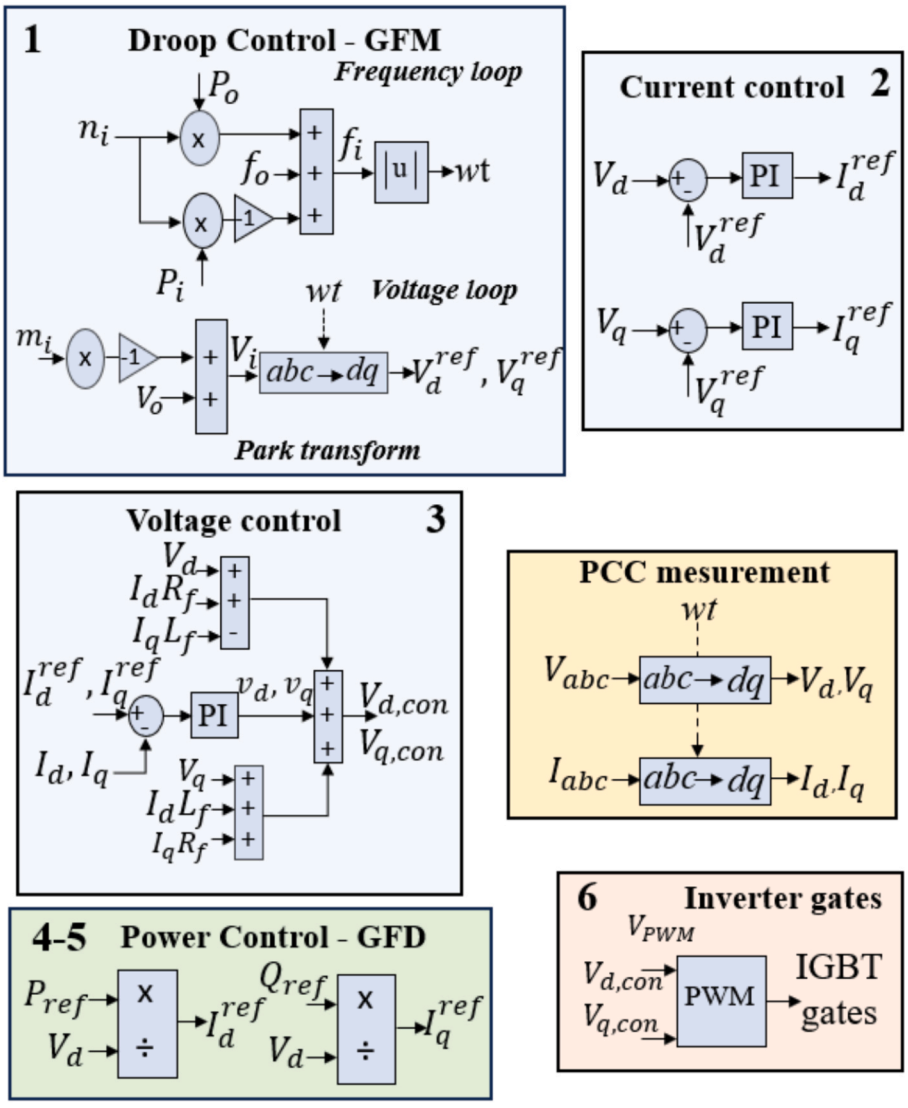

Fig. 2. MGC loops scheme control.

The subsequent control stage focuses on the current controller. Its purpose is to adjust the measured values of direct (I_d) and quadrature (I_q) current to track the predefined reference values. A PI controller is applied to reduce the difference between the measured and referenced signals. The control outputs from these PI controllers are denoted as $v_{d,i}$ and $v_{q,i}$, which correspond to the voltage controlled by each inverter. To ensure the interdependence of the direct and quadrature components, it is necessary to decouple these axes. This decoupling is achieved via feedforward decoupling, as outlined in the following equations:

$$V_{d,con} = V_d + I_d R_f - I_q L_f + v_{d,i} \tag{3}$$

$$V_{q,con} = V_d + I_d L_f + I_q R_f + v_{q,i} \tag{4}$$

where R_f and L_f represent the filter's resistance and inductance.

A conventional pulse width modulation (PWM) is employed by each inverter to generate output pulses. The modulation index (M) and the angle (Θ) are calculated using the expressions defined in Eqs. (5) and (6):

$$M = \left| \frac{V_{d.con}, V_{q.con}}{\frac{V_{DC}}{2} \frac{1}{\frac{V^*_{sec}\sqrt{2}}{\sqrt{3}}}} \right| \tag{5}$$

$$\theta = \angle \left(\frac{V_{d.con}, V_{q.con}}{\frac{V_{DC}}{2} \frac{1}{\frac{V^*_{sec}\sqrt{2}}{\sqrt{3}}}} \right) + wt \tag{6}$$

In this context, Θ denotes the phase angle of the PWM signal, V_{DC} represents the input direct voltage, and V^*_{sec} stands for the rated secondary voltage of the transformer. Finally, the PWM block is responsible for generating the activation signals for the inverter, thereby ensuring control over the voltage and frequency, as depicted in Fig. 2.

To adjust the cascade control method for the MG connected via a GFD inverter, a different approach is used. Initially, it is essential for these converters to synchronize precisely with the AC voltage at the PCC. This is accomplished by using a PLL. Following this, the traditional droop control and voltage regulation are substituted with a power controller. In this configuration, the reference values for active and reactive power (P and Q) are divided by V_d to derive the reference currents, I^*_d and I^*_q. These currents are subsequently used in the current control loop. The rest of the cascade control structure remains unchanged from the one employed for the GFM inverters.

3. Synchronization control scheme

This section outlines the optimal control scheme that ensures smooth synchronization between IS and GC modes. A control structure enabling operation in both modes is proposed, incorporating a synchronization loop as depicted in Fig. 3. Initially, a primary control based on traditional droop control is adopted for MGs connected through GFM inverters. For the MG connected via a GFD inverter, a local control based on the power to be injected by the MG is utilized. The secondary control offers two functions: it restores frequency values to the rated frequency in response to disturbances from the primary control and corrects voltage deviations to the MGC nominal value.

For this purpose, the secondary control has two different modes of operation. First, when switch S_a is in position 1 and switch S_b is also in position 1, this indicates that the MGC operates in IS mode. In this operational mode, the GFM inverters must generate and control the frequency and voltage according to the reference values. Specifically, the secondary control sets the reference values to f_{nom} for frequency and V_{nom} for voltage, respectively. Two independent PI controllers adjust the error between the measured frequency at the PCC (f_{PCC}) and the measured voltage (V_{PCC}). The outputs of these controllers provide the reference values of frequency (f_o) and voltage (V_o) , which are applied in Eqs (1) and (2), respectively, to restore the deviation produced in the droop control.

On the other hand, when switch S_a is in position 2 and switch S_b is also in position 2, the MGC operates in GC mode. In this operational mode, the main grid is responsible for maintaining voltage and frequency, and the MGC injects a specified power into the grid. Two independent PI controllers, one for active power and another for reactive power, are used to adjust the power injected at the PCC according to the reference values for active (P_{ref}) and reactive (Q_{ref}) power. The output signals of both PI controllers are used as the reference values for frequency and voltage for the secondary control in GC mode.

To interconnect a MGC into a main grid, usually considered as an infinite power grid, it is essential to achieve synchronization at the PCC. This synchronization involves aligning frequencies, voltage phases, and magnitudes at the PCC. Frequency discrepancies can be minimized due to the frequency restoration carried out by secondary frequency loops and the use of identical rated frequencies. However, the phase and magnitude differences in the PCC voltages must be controlled to be reduced as much as possible to ensure stability (Naderi et al., 2023).

In practical scenarios, achieving a perfect alignment in voltage amplitude, frequency, and phase angle to switch off a circuit breaker and synchronize with the main grid is a significant challenge. Consequently, the circuit breaker cannot be turned off precisely at that perfect synchronization point (Ransom, 2014). Instead, the control systems are designed within an acceptable tolerance range for variations in these three critical parameters. According to IEEE Std. 1547–2018 (Std, 2018), the voltage deviation between the MGC and the main grid must not exceed 5 % of the grid voltage. The frequency difference should be limited to 0.2 Hz. Moreover, the maximum permissible phase angle shift is 15 degrees. These parameters will be utilized to synchronize the MGC with the main grid and ensure supply quality during the transition.

To achieve a smooth synchronization that adheres to the aforementioned constraints, two independent control loops are employed. Two individual PLLs are used to express the measured voltages at the PCC (V_{PCC}) and the grid (V_{Grid}) in the dq frame. During the synchronization process, switches S_c and S_d are set to position 1. A PI controller adjusts the direct component of the MGC voltage (V_d^{PCC}) to match the direct component of the grid voltage (V_d^{Grid}), resulting in a new term, denoted as δ_V, which is added to the secondary control to align the MGC voltage with the main grid voltage. Similarly, another PI controller corrects the error between the quadrature component of the MGC voltage (V_q^{PCC}) and the quadrature component of the grid voltage (V_q^{Grid}). This results in a new term represented as δ_f, which is also included to the secondary control to align the frequency and phase angle with the main grid, facilitating a smooth synchronization. Once the synchronization is complete, the circuit breaker that connects the MGC to the main grid is closed, and both switches S_c and S_d are set to position 2.

4. Optimal synchronization differential evolution algorithm

In the literature, there are limited research on synchronization methods that facilitate a smooth transition to GC mode using both GFM and GFD inverters (Alrajhi, 2024). GFD inverters are capable of

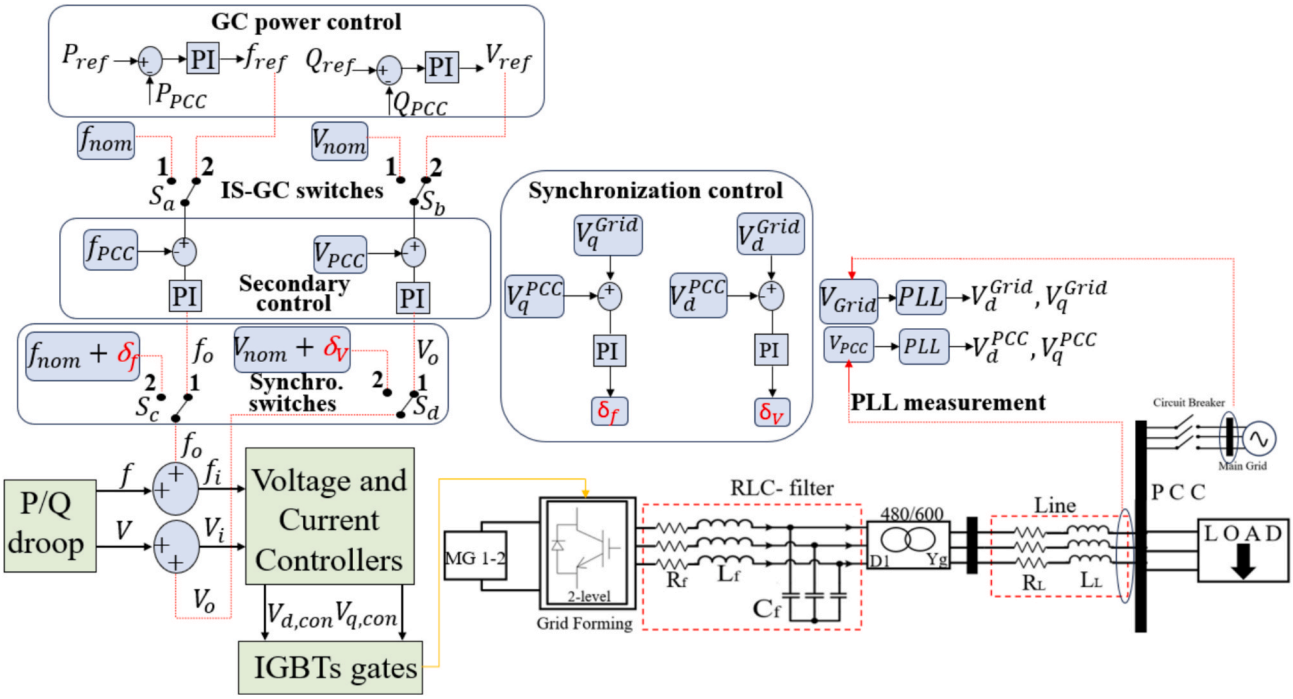

Fig. 3. Optimal synchronization control architecture.

regulating the voltage and frequency of isolated MGs, ensuring their stability and reliability even in the absence of the main grid. Regarding current advancements in converter-based MGs control methodologies and MGs synchronization strategies (IEEE Texas Power and Energy Conference (TPEC), 2020), some studies have explored the integration of battery energy storage systems (BESS) for power management. However, the effectiveness of this control scheme is constrained by the requirement that the capacity of the BESS connected to the inverter should be no less than 150 % of the MG's average power requirement (Talapur et al., 2018).

Unlike most studies proposed in the literature based on the variation of droop coefficients (Ganjian-Aboukheili et al., 2020; Shahab and Wang, 2021; Cao et al., 2023), this work introduces a novel and optimal approach, which is based on calculating the optimal power that the GFD inverter should inject to minimize the ITSE during the synchronization process. In the proposed approach, it is also possible to quantify the performance of the synchronization process, which is commonly overlooked in most studies (Khan et al., 2023; Hmad et al., 2019; Meng et al., 2023; Li et al., 2017), and keep the MG within its nominal capacity.

This section introduces an innovative DE algorithm specifically designed to enhance the smooth synchronization from IS to GC modes, with a primary focus on minimizing frequency deviations. The approach simultaneously manages the operation of both GFM and GFD inverters. The real-time objective function to be optimized is articulated in Eq. (7):

$$O.F = \min(\mathrm{ITSE}\,(\mathrm{f(t)}) \tag{7}$$

where ITSE (f(t)) represents the ITSE index for frequency control over time.

The expression for the frequency control error can be formulated as:

$$e(t) = f_{nom} - \mathrm{f} \tag{8}$$

Therefore, this main aim of this section is to introduce an expression to optimize the objective function proposed in Eq. (7), where the time-based error defined in Eq. (8). To this end, it is first necessary to consider that the total power supplied by the MGC must consistently satisfy the demand. The power balance can be expressed as follows:

$$P_{GFM}^{\mathrm{tot}} + P_{GFD} = P_{LOAD} \tag{9}$$

where P_{GFM}^{tot} represents the total power injected by the MG connected to a GFM inverter, P_{GFD} represents the power delivered by the MG connected to a GFD inverter, and P_{LOAD} is the power consumed by the load. Note that P_{GFM}^{tot} is obtained as the sum of the power of each MG connected to a GFM inverter.

Furthermore, the output power of the MGs is constrained between 0 and the rated power rating of the inverter to ensure operation within secure operational limits. The first MG, connected to GFM inverter (MG_1) is designed to deliver 500 kW, the second MG (MG_2) is rated for 250 kW, and the third MG, connected to a GFD inverter (MG_3), has a maximum capacity of 300 kW.

Therefore, based on the traditional droop control equation defined in Eq.(1), the term $P_{o,i}$ can be expressed as follows:

$$P_{o,i} = P_{f,max} + \frac{f_{max} - f_{nom}}{n_i} \tag{10}$$

where $P_{f,max}$ is the power at the highest frequency, and f_{max} is the highest allowable frequency.

By combining Eqs (1) and (10), the frequency can be expressed as follows:

$$f = (f_o + f_{max} - f_{nom}) + n_i(P_{f,max} - P_{GFM}^{\mathrm{tot}}) \tag{11}$$

The following modification for Eq. (8) can be derived by substituting the term for f obtained in Eq. (11) as follows:

$$\begin{aligned} \mathrm{e(t)} &= f_{nom} - (f_o + f_{max} - f_{nom}) + n_i(P_{f,max} - P_{GFM}^{\mathrm{tot}}) \\ &= 2f_{nom} - f_o - f_{max} - n_i(P_{f,max} - P_{GFM}^{\mathrm{tot}}) \end{aligned} \tag{12}$$

where the term P_{GFM}^{tot} can be substituted according to Eq. (9) to yield:

$$\mathrm{e(t)} = 2f_{nom} - f_o - f_{max} - n_i P_{f,max} + n_i P_{LOAD} - n_i P_{GFD} \tag{13}$$

Finally, the objective function proposed in Eq. (7) can be expressed in terms of the MGC frequency, the droop control coefficient, the demanded power, and the power injected by the GFD inverter:

$$\begin{aligned} \mathrm{O.F} &= \min(\mathrm{ITSE(t)}) \\ &= \min \int_0^T \sqrt{2f_{nom} - f_o - f_{max} - n_i P_{f,max} + n_i P_{LOAD} - n_i P_{GFD}} \cdot t\mathrm{dt} \end{aligned} \tag{14}$$

As a result, a novel objective function is presented, expressed with generic variables within the MGC, which can be easily adapted to other MGC configurations. This expression demonstrates how the frequency control error can be optimized based on the power injected by the MG operating with a GFD inverter, in contrast to the traditionally adopted approach of modifying the droop control coefficients, the disadvantages of which have been previously discussed.

In this regard, the proposed approach offers the following advantages: When the MGC operates in steady-state conditions, i.e., with a value off_o = 1pu (60 Hz), the control provides the optimal operating value for the MG connected to the GFD inverter. Moreover, when the synchronization process with the grid begins, the term f_o varies according to the deviations imposed by the secondary control to maintain the frequency around the established nominal value. In this context, the synchronization algorithm determines the new power reference that the GFD inverter should adopt in order to minimize the error during the synchronization process, thus preventing fluctuations that could compromise the MGC's operation and ensuring a transient response consistent with the values outlined in IEEE Std. 1547–2018.

In this paper, the DE algorithm is utilized to address the optimization problem previously introduced. The DE algorithm provides several advantages that differentiate it from other optimization techniques. Unlike more complex algorithms, such as genetic algorithms (Saxena et al., 2022), DE provides a simpler implementation. This is primarily due to the lower number of parameters that need to be adjusted compared to other algorithms, such as particle swarm optimization, where tuning the inertia coefficients may challenge the adjustment process (Zulueta et al., 2022). Furthermore, it does not require system linearization, unlike MPC methods (Fachini et al., 2024).

Due to its high computational efficiency, the DE algorithm is especially well-suited for addressing real-time optimization challenges and adapting to dynamic system variations. This makes it more advantageous compared to other optimization methods that rely on the derivative of the objective function or particle swarm optimization (Hou et al., 2024), such as (Abhinav et al., 2017), which can be difficult to obtain in transient operating conditions, such as during the grid synchronization process.

The DE algorithm is a population-based metaheuristic approach, inspired by natural evolutionary processes. It iteratively refines a set of candidate solutions through mutation, crossover, and selection mechanisms. At each iteration, the algorithm leverages a set of solutions to generate a new candidate by incorporating the differences between randomly selected vectors. Initially, a population of random solutions, denoted as $x_i(k)$, is generated, where i represents the solution index (ranging from 1 to N, the population size) and k denotes the current iteration.

For each solution, $x_i(k)$, a mutant vector, $v_i(k+1)$, is computed as follows:

$$v_i\,(k+1) = x_r1(k) + F{\cdot}(x_r2(k)\,) - (x_r3(k)\,) \tag{15}$$

where $v_i(k+1)$ is the mutated vector, $x_r1(k)$, $(x_r2(k)\,)$ and $(x_r3(k)\,)$ are randomly selected solutions, and F is a scaling factor that controls the mutation step size.

After mutations, crossover is applied to generate a candidate vector, $u_i(k+1)$ combining the mutated vector with the current solution, by

applying a crossover rate, CR, defined as:

$$u_i(k+1) = \left\{ \begin{array}{c} v_i(k+1), if rand() \le CR \\ x_i(k) if not \end{array} \right\} \quad (16)$$

Next, the objective function of the new solution, $u_i(k+1)$, is compared with that of the current solution, $x_i(k)$:

$$x_i(k+1) = \left\{ \begin{array}{c} u_i(k+1), iff(u_i(k+1) \le f(x_i(k)) \\ x_i(k) if not \end{array} \right\} \quad (17)$$

The flowchart of the DE operation is presented in Fig. 4. Moreover, the DE pseudocode is represented in Table 2.

The algorithm begins by initializing a population of individuals, with each representing a potential solution randomly distributed within the problem's defined search space. This initial diversity is crucial for ensuring broad exploration and avoiding premature convergence. Following initialization, the algorithm enters an iterative process consisting of three main operations: mutation, crossover, and selection.

In the mutation phase, new candidate solutions, referred to as mutant vectors, are generated by combining existing individuals from the population. Specifically, three distinct individuals are randomly selected, and a scaled difference between two of them is added to the third. This differential mutation introduces variability and helps the algorithm explore unexplored regions of the search space. Subsequently, the crossover operation creates trial vectors by mixing components of the mutant vectors with those of the current target individuals. This blending process is governed by a crossover probability, which balances exploration and exploitation by determining how much of the mutant vector's information replaces the original individual's traits.

After generating trial vectors, the algorithm evaluates their quality using the objective function. Through the selection step, each trial vector competes with its corresponding target vector. If the trial vector exhibits improved performance, it replaces the target vector in the population for the next generation. Otherwise, the target vector is retained. This elitist selection mechanism ensures that the population's overall fitness does not degrade over iterations, steadily guiding the search toward better solutions. The process of mutation, crossover, and selection repeats until the maximum number of iterations is achieved. This cyclical refinement enables DE to effectively balance global exploration and local exploitation, making it a robust and efficient optimization method.

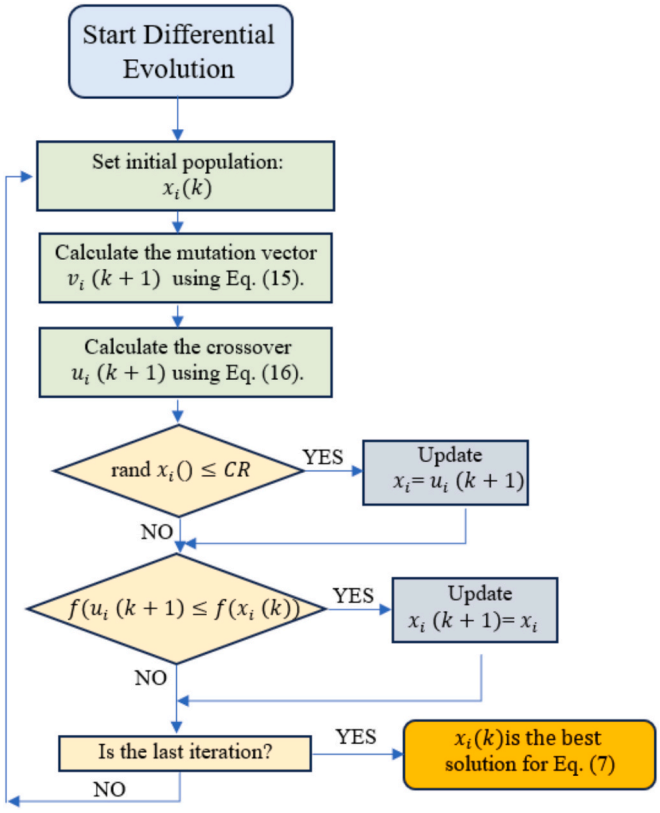

Fig. 4. DE algorithm flowchart.

Table 2
DE algorithm sequence.

Step 1:	Obtain the operational data from the MGC.
Step 2:	Starting population. The initial set of individuals is created through a random generation process as described below. For i = 1:m $x_i^{(0)} = \left[x_{i,1}^{(0)}, x_{i,2}^{(0)}, \cdots, x_{i,n}^{(0)}\right], i = 1, \cdots, m$ where m represents the number of individuals in the population and n denotes the problem's dimensionality
Step 3:	Differential mutation: For each candidate i, produce a mutant vector as follows: $v_i^{(k+1)} = x_{r1}^{(k)} + F \cdot (x_{r3}^{(k)} - x_{r3}^{(k)})$ where r_1, r_2, $r_3 \in \{1, \cdots, m\}$ are distinct from each other and not equal to i, and $F \in [0,1]$ is the scaling factor
Step 4:	Crossover. The trial vector $u_i^{(k+1)}$ is created by applying a crossover operation with a crossover probability $\in [0,1]$. An index j_0 is randomly selected from the set $\{1, \cdots, n\}$: For $j = 1 : n$ if rand $() \le CR$ or $j = j_0$ $u_{i,j}^{(k+1)} = v_{i,j}^{(k+1)}$ else $u_{i,j}^{(k+1)} = x_{i,j}^{(k)}$ end
Step 5:	Selection. The fitness of both $u_i^{(k+1)}$ and $x_i^{(k)}$ is assessed, and the vector with superior performance is chosen to proceed to the subsequent generation if $f\left(u_{i,j}^{(k+1)}\right) < f\left(x_i^{(k)}\right)$ $x_i^{(k+1)} = u_i^{(k+1)}$ else $x_i^{(k+1)} = x_i^{(k)}$ endend

The performance of the DE algorithm is governed by four key tuning parameters: the scaling factor (F), the crossover rate (CR), the population size (n_p), and the number of iterations (N). These parameters directly influence the mutation, crossover, and convergence behavior of the algorithm, making them critical to its effectiveness.

Specifically, the scaling factor (F) determines the amplification of the differential variation used in the mutation step, which affects the exploration capability of the algorithm. A value of $F = 0.75$ was selected to balance convergence speed and solution diversity, thereby avoiding premature convergence and ensuring stable search dynamics (Mallipeddi and Suganthan, 2010). The CR, used in the recombination step, controls the probability of mixing components between the mutant vector and the current candidate. A value of $CR = 0.9$ was chosen to encourage aggressive recombination, enhancing the global search and adaptability of the algorithm (Gao and Liu, 2012).

The population size ($n_p = 20$) defines the number of candidate solutions evaluated per generation. This value was selected to provide sufficient diversity for robust exploration of the search space while keeping computational cost compatibility with the sampling time of the control algorithm. Finally, the number of iterations ($N = 100$) sets the stopping criterion and reflects the trade-off between computational time and convergence accuracy. This value ensures convergence to an optimal or near-optimal solution within the time constraints of the application.

To appropriately tune the DE algorithm parameters, a comprehensive sensitivity analysis was conducted to evaluate the influence of each parameter on the control response. This analysis aimed to identify suitable values for n_p, F, and CR to ensure optimal frequency regulation performance. The ITSE was used as the performance metric, as it effectively penalizes deviations from the nominal frequency over time, providing a rigorous quantitative assessment of control quality.

The sensitivity analysis consisted of 250 independent simulations, where the values of n_p, F, and CR were randomly sampled within a

predefined range spanning from conservative to aggressive configurations. Specifically, n_p varied in the range [5, 50], F within [0.1, 1.0], and CR in the interval [0.1, 1.0]. These ranges were selected to capture the practical limits typically considered in DE-based optimization strategies, allowing for a robust comparison across parameter combinations.

The results of the sensitivity analysis are depicted in Fig. 5. Fig. 5a illustrates the influence of the population size n_p on the ITSE index. The results clearly indicate that a population size of 20 achieves consistently low ITSE values. Beyond this threshold, increasing n_p does not lead to further improvements in control performance, suggesting a point of diminishing returns in terms of population growth.

Fig. 5b Fig. 5b shows the impact of the scaling factor F on the ITSE. As observed, a value of $F = 0.75$ results in stable and minimal ITSE values. For lower values of F, significant fluctuations in the ITSE are noted, indicating reduced reliability and performance consistency. Therefore, F = 0.75 was selected as the most appropriate value for the proposed control application.

Finally, Fig. 5c presents the relationship between the crossover rate *CR* and the ITSE. The results reveal that small values of *CR* tend to hinder the algorithm's ability to explore new candidates, leading to optimization stagnation and suboptimal performance. Conversely, high values of *CR* enhance the algorithm's adaptability and result in lower ITSE values. Based on this evidence, a value of CR = 0.9 was adopted to ensure dynamic adaptation and maintain high-quality control performance.

5. Results and discussion

5.1. Synchronization general performance

This section presents the results of the DE-based synchronization seamless transition under normal operating conditions. Furthermore, to demonstrate the advantages offered by the proposed approach, a comparison is made with the commonly adopted approach based on varying the coefficients of droop control. The operating parameters of the MGC are detailed in Table 3.

Fig. 6 depicts the measurements taken at the PCC during the synchronization process. The overall operation is described as follows. The MGC operates in IS mode at the beginning of the simulation. At time t = 7 s, a command is sent to synchronize the MGC with the main grid. When the synchronization process is completed, which occurs at t = 12 s, the circuit breaker closes, and the MGC transitions to GC mode.

Fig. 6a shows the results of active power (P_{PCC}) and reactive power (Q_{PCC}). While operating in IS mode, P_{PCC} has a value of 315 kW, and Q_{PCC} has a value of 40 kVAr. When the MGC transitions to GC mode at t = 12 s, it connects to the main grid, injecting a power of 435 kW. At t = 18 s, the injected power increases to 515 kW. Regarding Q_{PCC}, it increases to 50 kVAr at t = 12 s upon synchronization with the grid. Additionally, another increase occurs at t = 16 s, reaching 90 kVAr. It can be observed that during the synchronization process, and during the changes made in GC mode, the control of P_{PCC} and Q_{PCC} remains stable without

Table 3
MGC parameters.

Symbol	Parameter	Unit
V_{nom}	Rated voltage	600 V
f_{nom}	Rated frequency	60 Hz
L_f	Filter inductance	1.08 mH
R_f	Filter resistance	1.08 mΩ
C	Filter capacitance	184 μF
Z_{LINE}	Transmission line parameters	5 mΩ + 1 mH
n_p	DE number of populations	20
N	DE number of iterations	100
CR	Crossover rate	0.9
n	Droop control coefficient	3 %

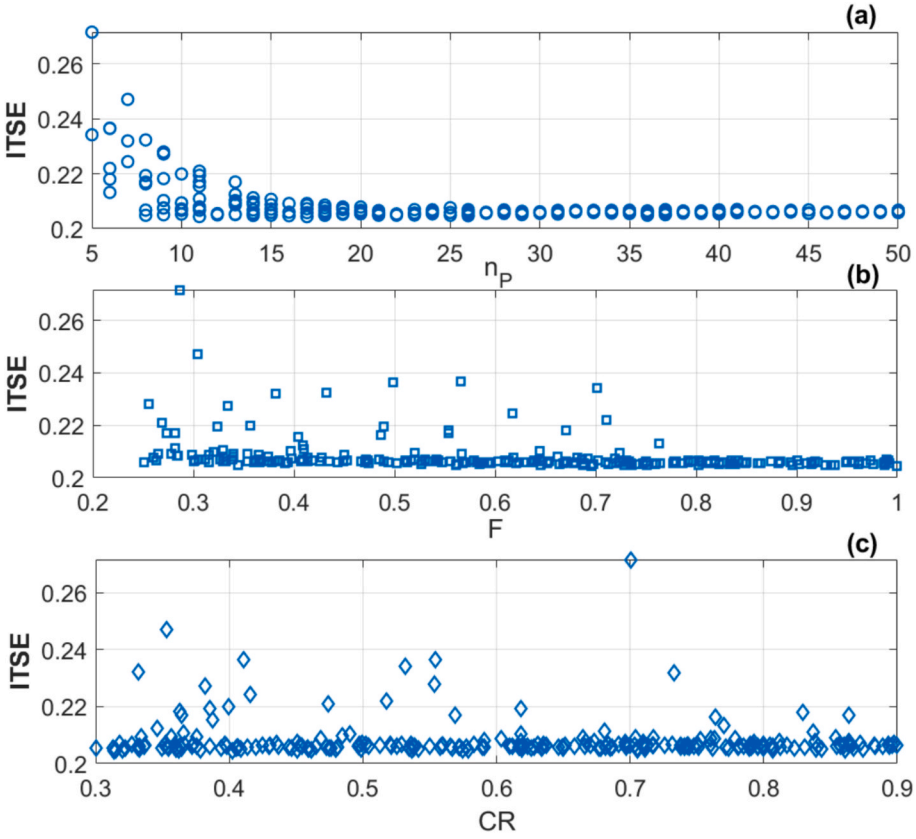

Fig. 5. Sensitivity analysis of DE algorithm parameters on frequency control performance using the ITSE index: (a) population size n_p, (b) scaling factor *F*, and (c) crossover rate *CR*.

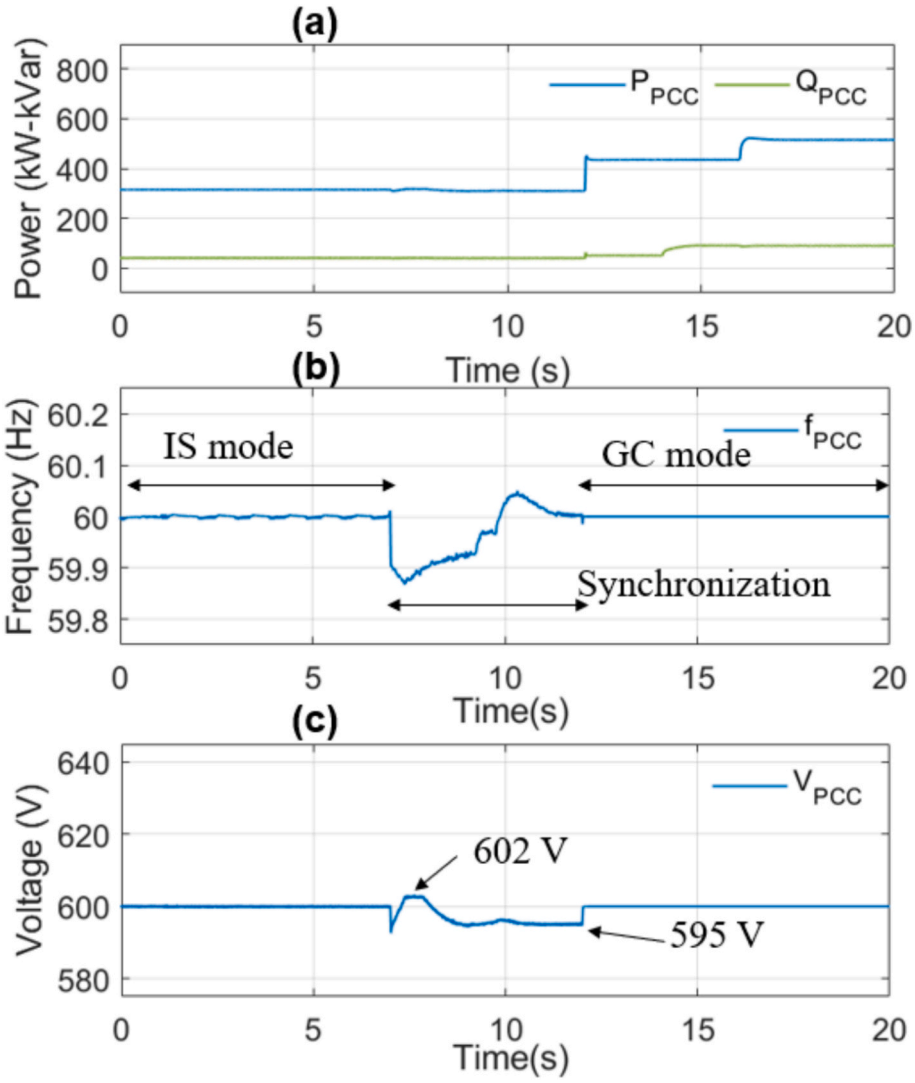

Fig. 6. DE optimal synchronization: (a) Active power (P_{PCC}), reactive power (Q_{PCC}), (b) PCC frequency (f_{PCC}), and (c) PCC voltage (V_{PCC}).

oscillations around the set value.

Fig. 6b shows the value of f_{PCC}. In IS mode, the MGC effectively controls the frequency at 60 Hz. When the synchronization process begins at t = 7 s, a slight drop in frequency is observed, reaching a minimum value of 59.87 Hz and a maximum value of 60.05 Hz. A remarkably smooth synchronization is achieved, with no transient oscillations observed throughout the transition.

Fig. 6c illustrates the value of V_{PCC}. Similarly, in IS mode, the MGC operates effectively at 600 V. During the synchronization process, the voltage drops to 595 V and experiences a maximum value of 602 V, where it can be appreciated the smooth transition for the voltage control.

According to IEEE Std. 1547–2018, when the aggregate rating of MG units (kVA) is 1000 kVA, as in the case study of this paper, the maximum allowed frequency deviation is 0.2 Hz, the allowed voltage deviation is 5 % of the nominal voltage, and the allowed angular deviation is 15°. The obtained results show a maximum difference in frequency control of 0.13 Hz, while the voltage deviation is 0.84 %. Therefore, the effectiveness of the control is confirmed according to IEEE Std. 1547–2018.

Fig. 7 shows the results of the active (Fig. 7a) and reactive (Fig. 7b) powers injected by each MG. The DE algorithm calculates the value of the power to be injected by MG_3 to minimize the frequency control error. During the operation in IS mode, the DE algorithm sets P_{GFD} at 148.33 kW for the given operating conditions. The remaining power to complete the balance up to 315 kW is distributed proportionally among the MGs operating with GFM inverters according to droop control, with P_{GFM1} = 111.38 kW and P_{GFM2} = 55.29 kW.

When the synchronization process begins, the value of P_{GFD} varies to minimize the frequency control error. The value of P_{GFD} progressively increases according to the value calculated by the DE algorithm, reaching 210 kW, and then returns to its original set value of 148.33 kW. As a result of this process, the power injected by MG_1 and MG_2 decreases simultaneously to maintain stable the power control. At t = 12 s, due to the load variation, P_{GFD} takes a value of 268.36 kW, while the values of P_{GFM1} and P_{GFM2} remain stable at 111.38 kW and 55.29 kW, respectively. Finally, when the injected power changes to 515 kW, P_{GFD} reaches its maximum value of 300 kW. Consequently, P_{GFM1} varies to 144.5 kW, and P_{GFM2} to 70.5 kW, effectively completing the active power balance. The reactive power balance is performed assuming that Q_{GFD} remains at 0 kVAr, with variations in reactive demand being handled by MG_1 and by MG_2. Fig. 7b illustrates the effective control in IS mode and the response to reference changes in GC mode.

Fig. 8 shows the line-to-line voltage values for one phase to facilitate the understanding of the synchronization process. In Fig. 8a, the line voltage of phase 'a' measured at the PCC (Va_{PCC}) and the line voltage of the same phase for the main grid (Va_{Grid}) are displayed. It can be observed that both voltages have the same amplitude of 600 V, but there is a phase difference between them. The synchronization process

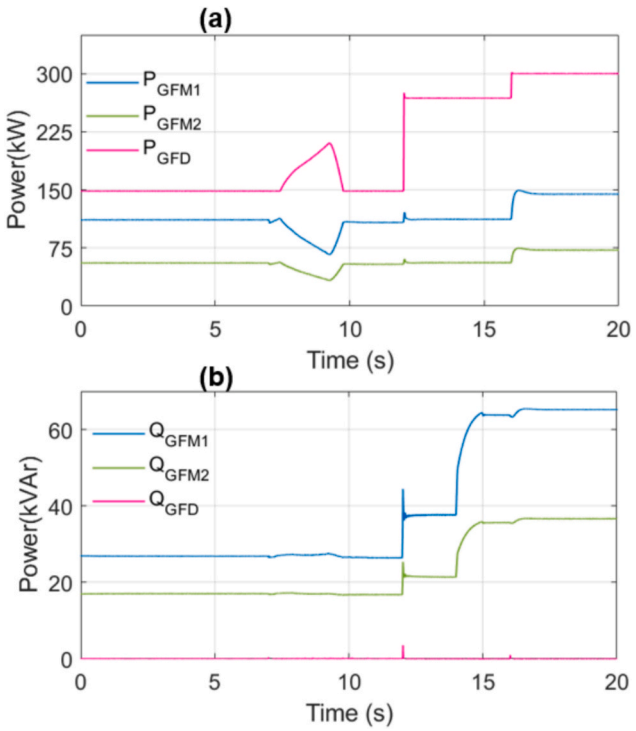

Fig. 7. MGC powers under normal operation: (a) Active MGs power, and (b) reactive MGs power.

optimally synchronizes both signals, as shown in Fig. 8b. Just before synchronization, from 11.93 s to 11.99 s, both signals are almost synchronized, which allows the MGC to transition smoothly from IS to GC at t = 12 s. The optimal ITSE value calculated for the proposed approach is 0.2208.

Fig. 8c shows the angles at PCC and at the grid. For GC mode, this angle for the grid voltages is $\theta_{Grid} = 30°$. For the MGC, the angle formed is $\theta_{PCC} = 100°$. During the synchronization process, the value of θ_{PCC} decreases until it perfectly aligns with the grid angle, thus complying with IEEE Std. 1547–2018 and ensuring a very smooth synchronization. Fig. 8d shows the control process during synchronization for the $V_{d,Grid}$ and $V_{d,PCC}$ components, and Fig. 8e depicts the $V_{q,Grid}$ and $V_{q,PCC}$ components, which correct the phase difference between the voltages measured at the PCC and the main grid.

To demonstrate the superiority of the proposed optimal control based on DE, the results are compared with the traditional approach that involves varying the droop control coefficients. For this, the DE algorithm presented in Section 4 is used to optimize the droop control coefficient (n) while keeping a constant power injected by the GFD inverter constant. Fig. 9 presents the synchronization results obtained using the traditional method based on varying the droop control coefficients.

Fig. 9a shows the results of P_{PCC} and Q_{PCC}, where a noticeable oscillation in the control of P_{PCC} can be observed at the moment of synchronization with the grid at t = 12 s. This is due to the fluctuations in the power injected by the MGs connected with GFM inverters, as the droop coefficients are adjusted, as shown in Fig. 9b. Fig. 9c presents the control of f_{PCC} during synchronization, while the V_{PCC} control is depicted in Fig. 9d. This approach also allows for acceptable frequency control, with the minimum frequency at 59.83 Hz and the maximum frequency at 60.05 Hz. In this scenario, the ITSE value is 0.3045, meaning the DE algorithm reduces the ITSE index by 37.91 %. Unlike the traditional approach, which relies on modifying the droop control coefficients of GFM inverters and induces oscillatory transients during synchronization (as shown in Fig. 9), Fig. 6 demonstrates that the proposed DE-based strategy significantly enhances the dynamic performance of the system. By dynamically adjusting the power reference of the GFD inverter, the DE algorithm achieves smoother synchronization, mitigating overshoot and abrupt variations in both frequency and voltage. This coordinated response enables more stable interaction with the GFM inverters and leads to superior supply quality.

Quantitatively, the DE-based approach reduces the ITSE index from 0.3045 to 0.2208, representing an improvement of 37.91 %. Furthermore, the maximum frequency deviation is limited to 0.13 Hz, while the voltage deviation remains within 0.84 %, both fully compliant with the

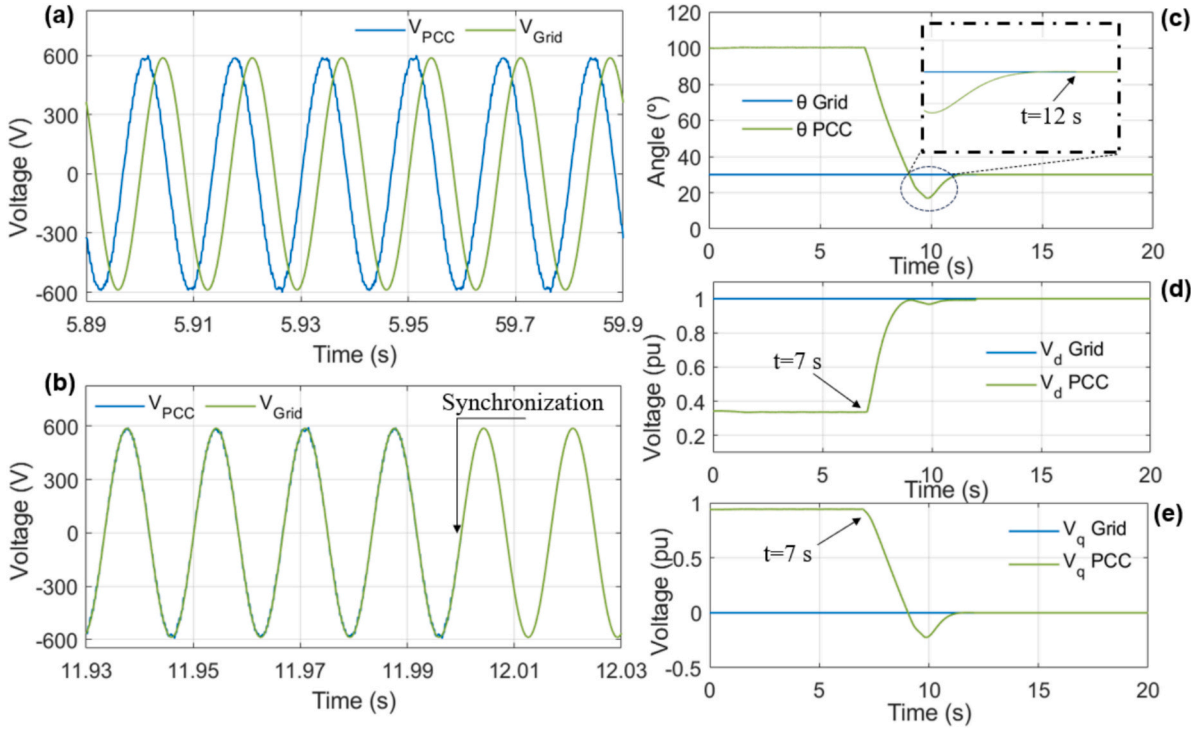

Fig. 8. IS MGC voltage, (b) Synchronization voltage, (c) Angle, (d) V_d voltage control, and (e) V_q voltage control.

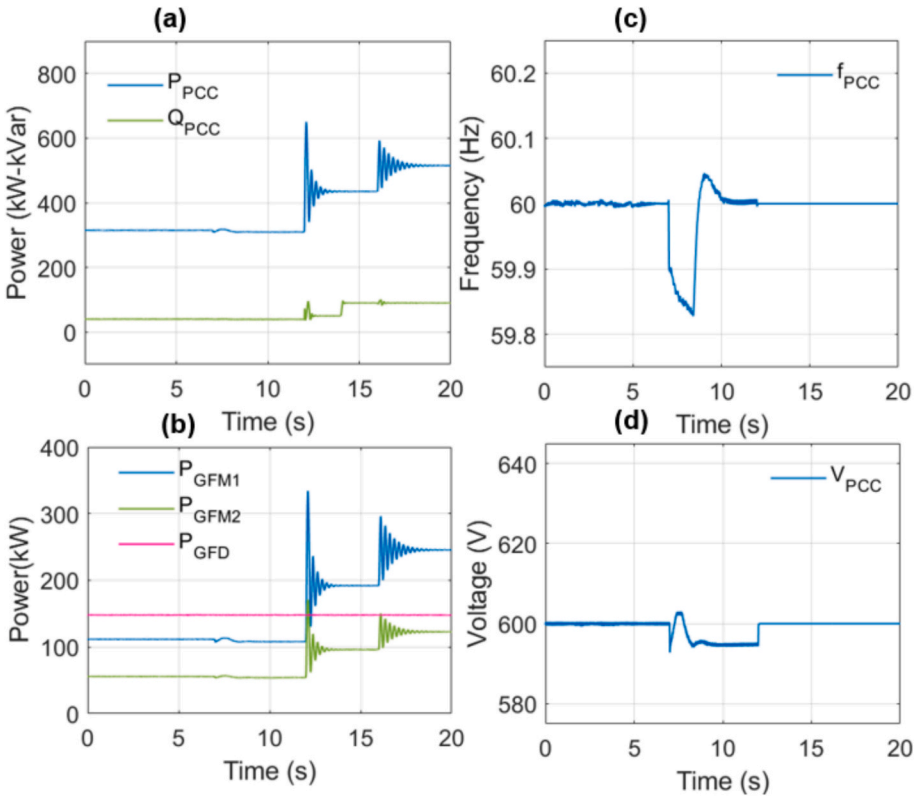

Fig. 9. Droop control synchronization: (a) Active power (P_{PCC}) and reactive power (Q_{PCC}) at the PCC, (b) MG_1 active power (P_{GFM1}), MG_2 active power (P_{GFM2}), MG_3 active power (P_{GFD}), (c) PCC frequency (f_{PCC}), and (d) PCC voltage (V_{PCC}).

requirements of IEEE Std. 1547–2018. These results confirm the effectiveness and robustness of the proposed control strategy under dynamic grid synchronization conditions.

Although the proposed synchronization control scheme and the optimal synchronization DE algorithm have shown a satisfactory performance under the tested conditions, certain limitations must be acknowledged, particularly regarding their scalability and practical applicability in larger or more complex MG configurations.

From a control standpoint, the synchronization scheme assumes timely and reliable communication among distributed MG units for the exchange of frequency, voltage, and power data. However, in real-world deployments, communication networks may introduce non-negligible delays, data loss, and clock misalignments. These issues can degrade synchronization performance, introduce transient deviations, or even compromise stability, especially in scenarios with rapidly changing loads or generation patterns. Future research could address the impact of communication latency and uncertainty, particularly in highly distributed or heterogeneous MG systems.

On the optimization side, the DE algorithm requires iterative evaluation of multiple candidate solutions per generation, which increases computational complexity as the number of MGs and decision variables grows. This computational cost may challenge the feasibility of real-time implementation, particularly on embedded platforms or in systems with strict timing constraints. Additionally, the algorithm's performance is sensitive to parameter tuning (e.g., mutation factor, crossover probability, population size), and suboptimal choices can affect convergence speed and solution robustness. These characteristics must be carefully considered when extending the proposed approach to larger MG clusters with higher degrees of operational variability.

5.2. Comparison against an fmincon based synchronization algorithm

To highlight the effectiveness of the proposed DE algorithm in achieving optimal synchronization, this section provides a comparative analysis between the DE-based approach and a conventional nonlinear optimization method implemented using the fmincon solver.

The fmincon algorithm is a gradient-based nonlinear optimization tool. It is designed to minimize a scalar objective function subject to both linear and nonlinear equality and inequality constraints, as well as upper and lower bounds on decision variables. It employs various numerical techniques—such as interior-point methods, sequential quadratic programming, and trust-region reflective approaches—to identify local optima in problems where both the objective and constraint functions are assumed to be continuous and differentiable (Al-butti and Altinoz, 2023). The fmincon formulation is presented in Table 4.

Fig. 10 presents the synchronization results obtained using the fmincon algorithm under the same scenario described in Fig. 6. In Fig. 10a, the active and reactive powers at the PCC (P_{PCC}, Q_{PCC}) are shown, illustrating effective control of both power components while maintaining system stability before, during, and after synchronization with the grid. Fig. 10b depicts the frequency measured at the PCC (f_{PCC}). For this optimization algorithm, a larger deviation is observed at the synchronization instant, with a minimum frequency of 59.8 Hz during the transient. This contrasts with the 59.87 Hz achieved by the DE algorithm. This difference results in an ITSE value of 0.3329 for fmincon, whereas the DE algorithm attains a lower ITSE of 0.2208. Consequently, the DE algorithm improves control performance by approximately 66.33 %, highlighting its suitability for the synchronization process and its ability to reach a more optimal solution. These improvements are attributed to DE's population-based search mechanism, which enhances global exploration and its robustness against convergence to local minima. Finally, Fig. 10c shows the line voltage at the PCC (V_{PCC}). The maximum voltage deviation reaches 593 V, which is very close to the 595 V observed with the DE algorithm. However, despite being a viable alternative, the fmincon algorithm exhibits overall inferior performance compared to the proposed DE method, as evidenced by the increment in

Table 4
fmincon algorithm sequence.

Step	Procedure
1	Define objective function: $O.F = \min(ITSE(t)) = \min \int_0^T t \cdot \sqrt{2f_{nom} - f_o - f_{max} - n_i P_{f,max} + n_i P_{LOAD} - n_i P_{GFD}}\ dt$
2	Define decision variables and bounds: $x = [P_{GFD}(t_1), \cdots P_{GFD}(t_n)]$ with $P_{GFD}^{min} \leq P_{GFD} \leq P_{GFD}^{max}$
3	Specify constraints: $c(x) \leq 0$
4	Initialize solution vector x_0 as initial guess for P_{GFD} over time horizon T
5	Employ nonlinear programming solver to iteratively minimize the objective function subject to constraints and bounds, updating x until convergence criteria are met.
6	Extract optimal power trajectory x_{opt} corresponding to minimized ITSE; validate solution feasibility and performance through simulation or experimental verification.

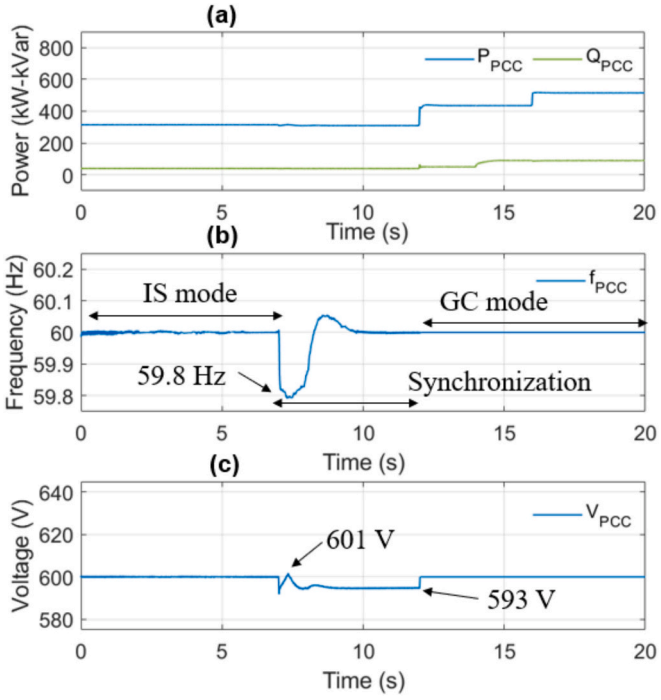

Fig. 10. Fmincon synchronization: (a) active power (P_{PCC}), reactive power (Q_{PCC}), (b) PCC frequency (f_{PCC}), and (c) PCC voltage (V_{PCC}).

the ITSE value and the more pronounced frequency drop.

5.3. Comparison against a PSO synchronization algorithm

To further assess the performance of the proposed DE-based synchronization algorithm, a comparative analysis with another widely used metaheuristic technique—Particle Swarm Optimization (PSO)—is presented in this section. PSO is a population-based stochastic optimization algorithm inspired by the social behavior of bird flocks and fish schools. It searches for optimal solutions by iteratively updating the position and velocity of each particle (candidate solution) in the search space, guided by both its own best-known position and the global best-known position found by the swarm. Table 5 represents the implemented PSO pseudocode.

Fig. 11 presents the synchronization results obtained using PSO, DE and fmincon optimization algorithms under identical test conditions. The three subplots provide a detailed view of the system dynamics during the synchronization process. In Fig. 11a, the P_{PCC} and Q_{PCC} are shown. PSO achieves effective power control, ensuring a smooth and stable transition before, during, and after synchronization. The control objectives for power balancing are clearly met by both DE and PSO methods, indicating that both algorithms are capable of producing dynamically valid solutions.

Fig. 11b illustrates the evolution of f_{PCC}. A slight deviation is observed during the transient, with both algorithms reaching a minimum of 59.87 Hz, which remains within acceptable synchronization margins. However, DE exhibits a smoother frequency response, resulting in a marginally lower ITSE of 0.2208, compared to 0.222 for PSO. This corresponds to a 0.45 % improvement, highlighting the DE algorithm's superior performance in penalizing frequency deviations over time, especially during transients. Fig. 11c shows the results of V_{PCC}. The voltage remains well regulated, with maximum deviations of 592 V for DE and 602 V for PSO. This confirms that both algorithms ensure voltage stability under dynamic conditions.

Beyond the frequency and voltage performance, the detailed comparison of key error indices in Table 6 further reinforces the advantages of DE. While the mean relative error (MRE) is virtually identical for both algorithms ($1.421 \cdot 10^{-4}$ vs $1.424 \cdot 10^{-4}$), DE maintains a marginally lower value, confirming slightly more accurate tracking in relative terms.

In terms of integral time-weighted absolute error (ITAE) and integral absolute error (IAE), DE again performs better, with ITAE = 2.826 and IAE = 0.2698, compared to PSO's ITAE = 2.832 and IAE = 0.2703. Although the improvements are modest (0.21 % in ITAE and 0.19 % in IAE), they are consistent and indicate that DE delivers smoother and more accurate trajectory tracking over time, especially in systems where long-term deviations are penalized. Similarly, the integral squared error (ISE) is slightly lower for DE ($2.186 \cdot 10^{-2}$) than for PSO ($2.195 \cdot 10^{-2}$), yielding a 0.41 % improvement, which reflects better overall damping and energy efficiency of the control action.

An additional and highly relevant advantage of DE lies in its computational efficiency. DE achieves the optimal solution in 3.45 min, while PSO requires 4.15 min, resulting in a 20.29 % reduction in PC simulation execution time. This becomes especially important in real-time control environments or hardware-in-the-loop implementations, where fast convergence is critical. Moreover, DE only requires the tuning of two parameters (F and CR), in contrast to PSO which depends on three (w, c_1, and c_2). This makes the calibration of DE not only more straightforward but also more robust against poor tuning choices. This simplicity in parameterization enhances the algorithm's practical applicability and adaptability to different scenarios. Although both DE and PSO reach stable and dynamically valid synchronization solutions, the DE algorithm consistently outperforms PSO across all evaluated metrics, achieving lower errors, faster convergence, and simpler implementation.

5.4. Sensitivity analysis

To demonstrate the robustness of the proposed synchronization control, this section presents a sensitivity analysis to variations in demand. The sensitivity analysis helps establish how the variability of P_{LOAD} influences the ITSE results. For this, 500 simulations are conducted, where the value of P_{LOAD} is randomly varied within a range between 150 and 500 kW, and the ITSE values for each measurement are recorded. Fig. 12 represents the ITSE values obtained in relation to the variations in P_{LOAD}. The ITSE values for the 500 simulations are shown in

Table 5
PSO algorithm sequence.

Step	Procedure
1	Define objective function: $O.F = \min(ITSE(t)) = \min \int_0^T t \cdot \sqrt{2f_{nom} - f_o - f_{max} - n_i P_{f,max} + n_i P_{LOAD} - n_i P_{GFD}}\ dt$
2	Define the vector of power trajectories: $x = [P_{GFD}(t_1), \cdots P_{GFD}(t_n)]$ with bounds $P_{GFD}^{min} \leq P_{GFD} \leq P_{GFD}^{max}$ k = 1,…,N
3	Initialize a swarm of M particles $x_i \in \mathbb{R}^N$ with velocity vectors v_i. Each particle denotes a candidate solution
4	Evaluate the objective function in step 1 (x_i) for each particle and update
5	Update velocity and position of each particle according to: $v(k+1) = w \cdot v^k + r_1 c_1 (x_{pbest}{}^k - x^k) + r_2 c_2 (g_{pbest}{}^k - x^k)$ where w is the inertia weight, c_1 and c_2 are acceleration coefficients, and r_1, $r_2 \in (0,1)$ are random numbers
6	Iterate steps 4 and 5 until convergence criteria are met (maximum number of iterations or minimal improvement in objective function)
7	Select the optimal solution $x^* = g$ yielding the minimum ITSE. Validate the optimal power trajectory $P_{GFD}(t)$ through simulation or experimental tests

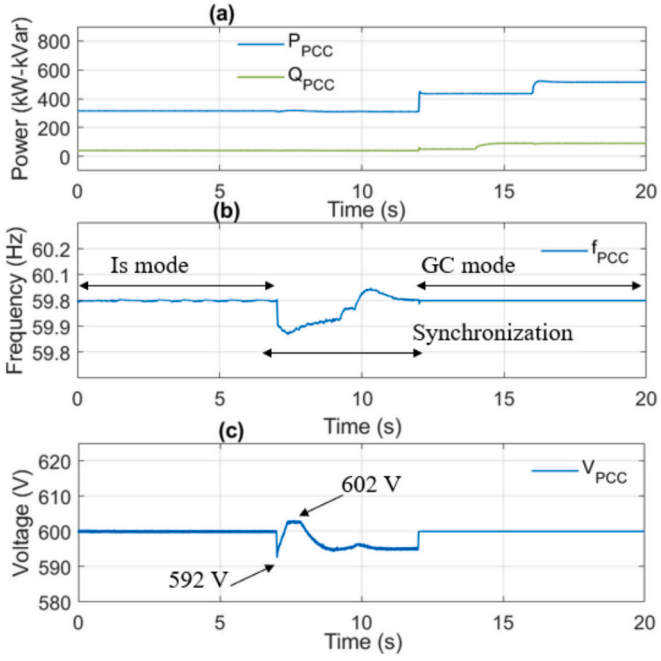

Fig. 11. PSO synchronization: (a) Active power (P_{PCC}), reactive power (Q_{PCC}), (b) PCC frequency (f_{PCC}), and (c) PCC voltage (V_{PCC}).

Table 7, with the ITSE defined within a range from a minimum value ($ITSE_{min}$) of 0.1937 to a maximum value ($ITSE_{max}$) of 0.362, with an average value ($ITSE_{avg}$) of 0.2459, a standard deviation ($ITSE_{sd}$) of 0.041, and a statistical mode ($ITSE_m$) of 0.2311. These results demonstrate the effectiveness and resilience of the control under a wide range of operating conditions, showing that varying the power of an MG connected to a GFD inverter can smooth and optimize the error in the synchronization process of an MGC.

5.5. DE synchronization under fault operation

Ensuring fault tolerance is a fundamental aspect in the development of control strategies for MGCs. This section highlights the fault resilience of the DE-based synchronization control. Fig. 13 depicts a 30 s simulation in which a fault occurs in MG_2 during GC mode. Initially, from t = 0 s to t = 12 s, the system operates in IS mode. At t = 15 s, a failure occurs

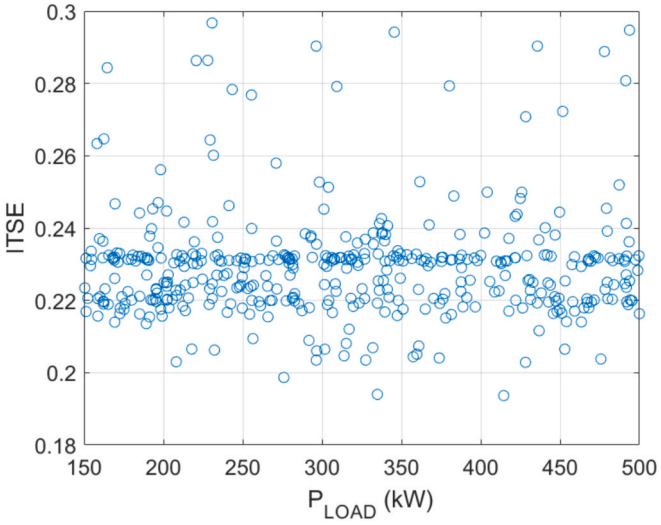

Fig. 12. Sensitivity analysis: ITSE under variations in..P_{LOAD}

Table 7
Sensitivity analysis results under load variability.

Parameter	Description	Value
$ITSE_{min}$	Minimum ITSE	0.1937
$ITSE_{max}$	Maximum ITSE	0.362
$ITSE_{avg}$	Average ITSE	0.2459
$ITSE_{sd}$	Standard desviation ITSE	0.041
$ITAE_m$	Statistical mode ITSE	0.2311

Table 6
Comparative performance of DE and PSO algorithms in synchronization control.

Parameter	Description	DE	PSO	Variation
t	Computation time	3.45	4.15	20.29 (%)
MRE	Mean relative error	$1.421 \cdot 10^{-4}$	$1.424 \cdot 10^{-4}$	0.21 (%)
ITAE	Integral time-weighted absolute error	2.826	2.832	0.21 (%)
ITSE	Integral time-weighted squared error	0.2208	0.222	0.45 (%)
IAE	Integral absolute error	0.2698	0.2703	0.19 (%)
ISE	Integral squeared error	$2.186 \cdot 10^{-2}$	$2.195 \cdot 10^{-2}$	0.41 (%)

in MG_2, resulting in its disconnection while MG_1 and MG_3 remain connected to the grid. In response to this fault, the system operator decides to isolate the MGC from the main grid at t = 20 s. In this scenario, MG_1, connected to a GFM inverter, assumes responsibility for maintaining stable voltage and frequency control.

Fig. 13a presents the results for P_{PCC} and Q_{PCC}. The MGC supplies a load of 235 kW and 50 kVAr in IS mode. Upon synchronization with the grid and transitioning to GC mode, the system delivers 315 kW, remaining stable both before and after the fault in MG_2. Furthermore, when it returns to IS mode at t = 20 s, the power control remains effectively maintained at 315 kW, despite the fault and the mode shift from GC to IS mode.

The synchronization process for f_{PCC} and V_{PCC} is shown in Fig. 13b and 13c, respectively. The minimum value achieved for f_{PCC} is 59.9 Hz, while the minimum V_{PCC} is 595 V, further demonstrating compliance with IEEE Std. 1547–2018.

The active and reactive powers delivered by each MG during the fault scenario are shown in Fig. 14a and Fig. 14b, respectively. Fig. 14a illustrates the optimal synchronization process, where the value of P_{GFD} is adjusted from 68.29 kW to 124.12 kW, while P_{GFM1} and P_{GFM2} droop from 111.24 kW and 55.47 kW to 77.37 kW and 35.39 kW, respectively. Once synchronized with the grid, P_{GFD} increases to 148.24 kW, P_{GFM1} rises to 130.18 kW, and P_{GFM2} balances the power with 36.58 kW. When the fault occurs in MG_2, P_{GFM2} drops to zero, and P_{GFM1} increases to 166.76 kW to maintain power balance. Fig. 14b shows the effective reactive power control, where Q_{GFD} is maintained at 0 kVAr, while Q_{GFM1} increases when the fault occurs in MG_2 at t = 15 s, with Q_{GFM1} set to 0 kVAr.

5.6. Hardware-in-the-loop experimental validation

This section presents a hardware-in-the-loop (HIL) real time verification to demonstrate the practical implementation of the proposed DE synchronization optimal control. HIL experimentation is a real-time testing methodology that integrates physical hardware components with simulated environments, enabling the validation of control

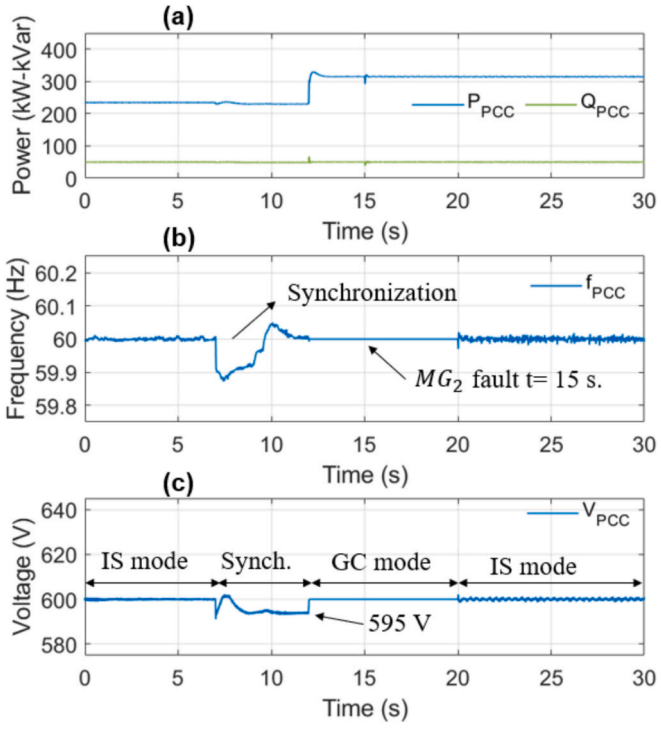

Fig. 13. MGC at fault operation: (a) Power at PCC, (b) frequency and (c) voltage.

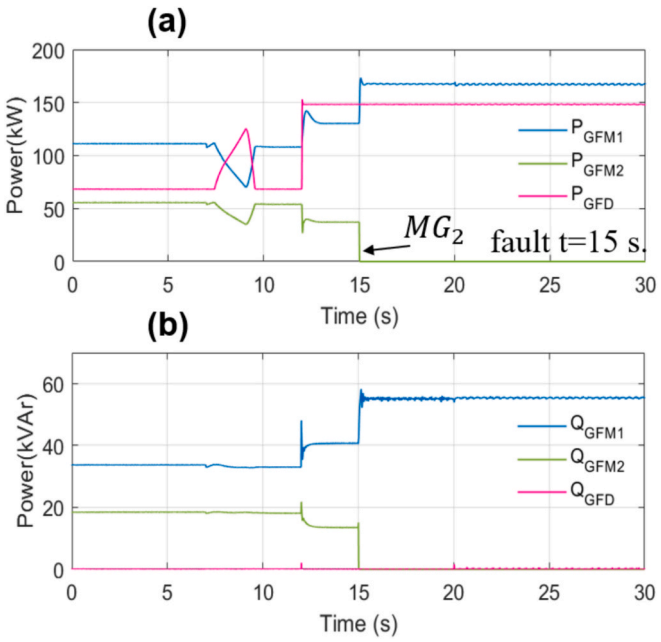

Fig. 14. MGC powers under fault operation: (a) Active MGs power, and (b) reactive MGs power.

algorithms and system behavior under realistic operating conditions without the need for full-scale prototypes (Pashaei et al., 2024). Fig. 15 provides an overview of the experimental setup, which includes the dSPACE MicroLabBox controller, the OPAL-RT4512 device, the host PC running RT-Lab, the analog input–output cards, and the DLM4038 oscilloscope.

In this configuration, the system operates in real-time using the OPAL-RT4512 unit, which is controlled and monitored through the RT-Lab software. This software enables both the programming and real-time observation of the plant's behaviour. With four 3.7 GHz cores, the OPAL-RT4512 unit executes the simulation with a time step of 50 μs, ensuring high-performance operation of the system.

The dSPACE MicroLabBox controller is responsible for executing the DE algorithm and transmitting the reference values of P_{GFD} to the OPAL-RT4512 unit. Communication between these devices is established through a series of analog input and output channels, operating within a voltage range of + 16 V/-16 V. The results of the simulation are then displayed on a DLM4038 digital oscilloscope.

A real-time simulation, replicating the fault scenario outlined in Section 5.5, is shown in Fig. 16. In Fig. 16a, the experimental measurements of P_{PCC} (represented by the blue signal) and Q_{PCC} (shown by the green signal) are displayed. The signals are plotted with a time scale

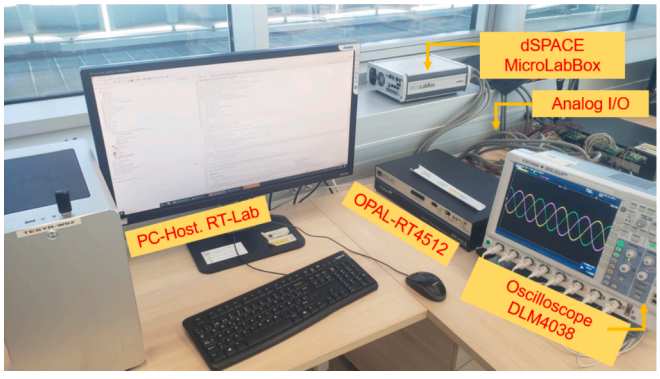

Fig. 15. Experimental HIL setup formed by OPAL-RT4512, dSPACE MicroLabBox, Oscilloscope DLM4038 and PC-Host.

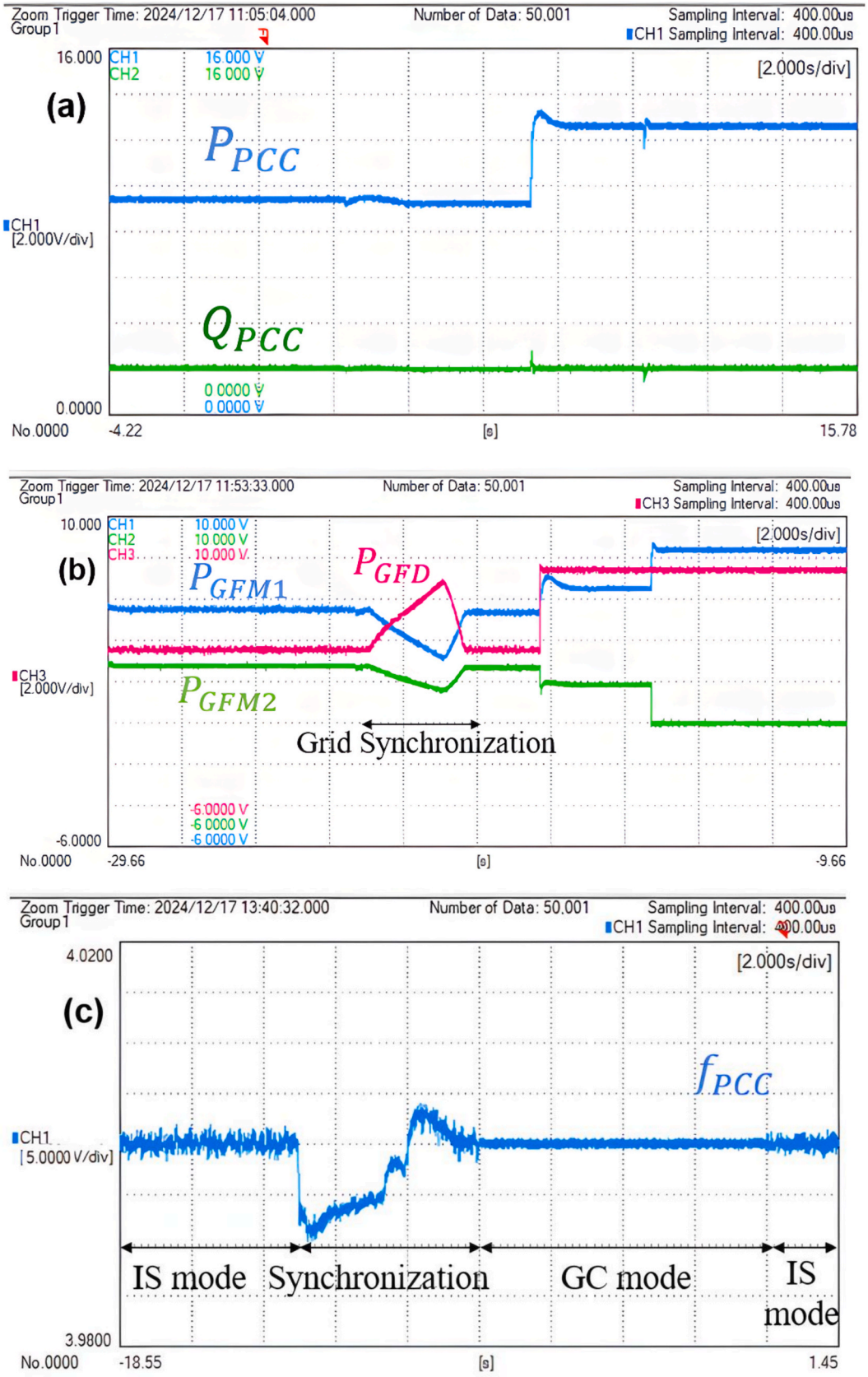

Fig. 16. Experimental results: (a) Active (P_{PCC}) and reactive power (Q_{PCC}) at PCC, (b) MGs active power (P_i), (c) frequency at PCC, (d) voltage at PCC (V_{PCC}) and (e) voltage waveform at PCC (..$V_a - V_b - V_c$)

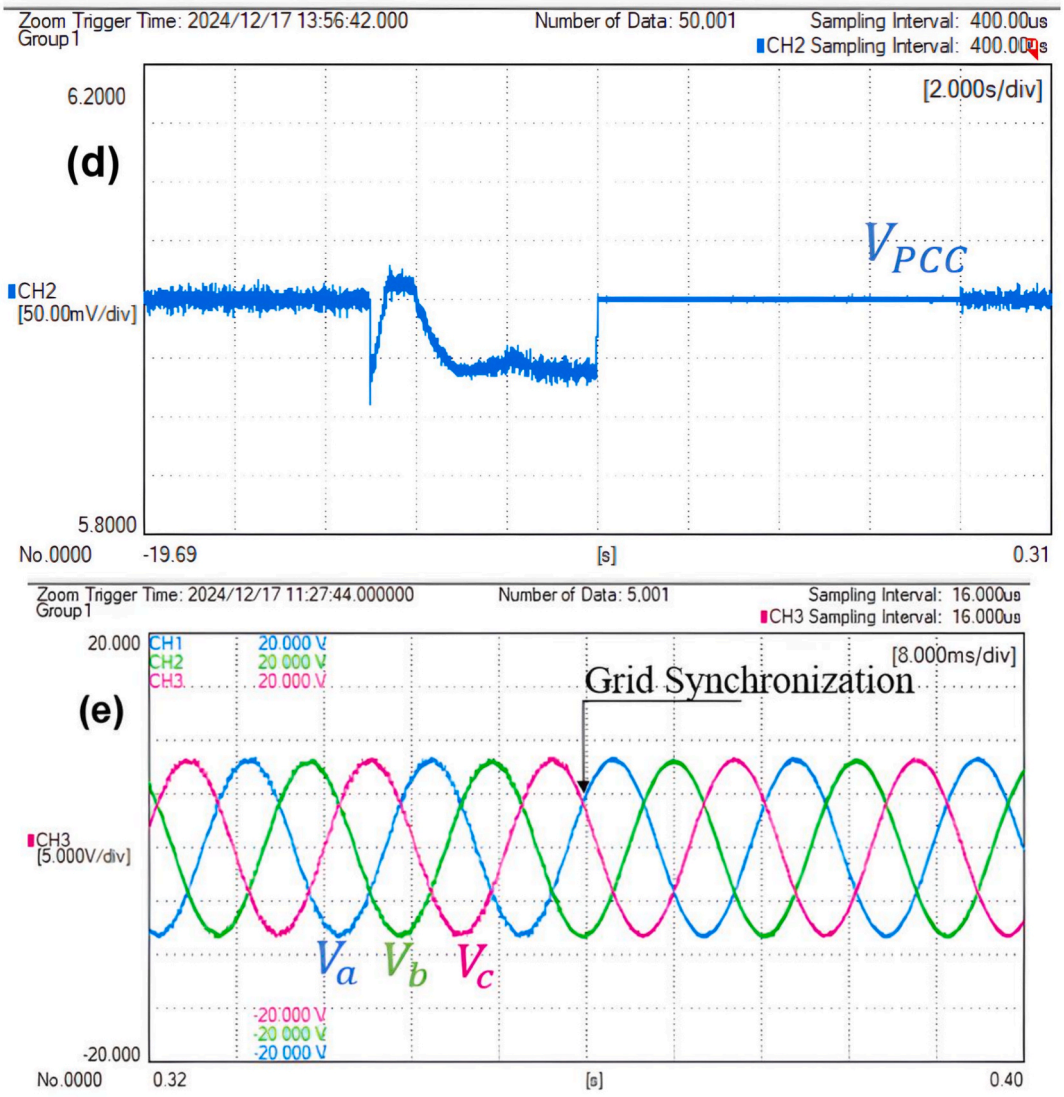

Fig. 16. (*continued*).

of 2 s/div and a voltage scale of 1 V/div for precise representation. Initially expressed in per unit (pu), the signals are amplified by a factor of 40 for proper visualization. Consequently, the P_{PCC} signal measures 9.4 V, which corresponds to 235 kW, while the Q_{PCC} signal registers 2 V, equivalent to 50 kVAr.

The experimentally measured active power values for each MG are shown in Fig. 16b. The figure is presented with a time scale of 2 s/div and a voltage scale of 2 V/div. For improved clarity, the power values are expressed in per unit (pu) and scaled by a factor of 50. The base power for P_{GFM1} (blue signal) is 500 kVA, for P_{GFM2} (green signal) it is 250 kVA, and for P_{GFD} (pink signal) it is 300 kVA. During the synchronization phase, P_{GFD} rises from 3.42 V (68.29 kW) to 6.21 V (124.12 kW), which is consistent with the simulation results presented in Section 5.5.

Fig. 16c illustrates the frequency measured at the PCC (f_{PCC}). The plot uses a scale of 2 s/div and 5 mV/div. During operation in IS mode, a measurement of 4 V corresponds to 60 Hz. As synchronization begins, the frequency drops to 59.87 Hz, which aligns with the experimentally measured 3.991 V. Finally, at t = 10 s into the real-time simulation, synchronization with the grid occurs, and the frequency returns to 4 V. This value remains stable until t = 18 s in the experimental simulation when the system switches back to IS mode.

The voltage at the PCC, denoted as V_{PCC}, is shown in Fig. 16d. The signal in this figure is plotted with a time scale of 2 s/div on the horizontal axis and a vertical scale of 5 V/div. A value of 6 V corresponds to 600 V of V_{PCC} throughout the entire simulation. During the synchronization process, the voltage decreases to 595 V, with an experimental reading of 5.95 V, which aligns with the results obtained in Section 5.3.

Finally, the three-phase sinusoidal waveforms of the voltage measured at the PCC are shown in Fig. 16e. In this case, a time scale of 8 ms/div and a vertical scale of 5 V/div are used. It can be observed that at the moment of synchronization with the grid, the waveform remains stable due to the smooth synchronization process proposed in this work.

The experimental outcomes confirm both the real-time functionality and the consistency of the proposed DE-based synchronization control. Moreover, they corroborate the results derived from time based on simulations, highlighting the practical viability of the suggested synchronization method.

To facilitate comparison between the results obtained from the simulation in Section 5.5 (see Fig. 14) and the HIL experimental results presented in Section 5.6 (see Fig. 16), Table 8 has been included. This table summarizes the key values for frequency, voltage, and power, along with their corresponding measurements acquired using the DLM4038 digital oscilloscope. The results demonstrate that the real-

Table 8
Comparaison of simulation and HIL results.

Variable	Simulation results	HIL OPAL-RT 4512 results
Steady state frequency	60 Hz	4 V[1 V- 15 Hz]
Synchronization frecuency	59.87 Hz	3.991 V[1 V – 15 Hz]
Steady state voltage	600 V	6 V[1 V – 100 V]
Synchronization voltage	595 V	5.95 V[1 V – 100 V]
Steady state P_{GFM1}	111.24 kW	5. 56 V[1 V – 20 kW]
Synchronization P_{GFM1}	70.37 kW	3.51 V[1 V – 20 kW]
Steady state P_{GFM2}	55.47 kW	2.77 V[1 V – 20 kW]
Synchronization P_{GFM2}	35.39 kW	1.77 V[1 V – 20 kW]
Steady state P_{GFD}	68.29 kW	3.42 V[1 V – 20 kW]
Synchronization P_{GFD}	124.12 kW	6.21 V[1 V – 20 kW]

time experimental outcomes, even under a critical fault involving a fault, successfully replicate the simulated values, thereby confirming the accuracy and validity of the obtained results.

6. Conclusions

This research advances the state of the art in MG synchronization by developing an innovative control approach based on the real-time implementation of a DE algorithm. The principal contribution lies in the design of a novel synchronization control framework that enables the MGC to dynamically regulate the power output of the MG through a GFD inverter, without requiring modifications to the traditional droop coefficients. This method significantly enhances synchronization accuracy and system stability during transitions between islanded and grid-connected modes.

The proposed control strategy departs from conventional methods by adjusting power injection directly for a GFD based on MG, rather than modifying droop coefficients. This not only simplifies implementation but also delivers improved synchronization performance. This approach also enhances the system's ability to adapt effectively to changing operating conditions and disturbances.

The performance gains are supported by thorough evaluation. The DE-based controller achieves a 37.91 % reduction in ITSE compared to classical droop control, confirming its superior error minimization capability. Moreover, when compared to a fmincon-based optimization approach, the DE algorithm demonstrates an additional 66.33 % improvement in ITSE, underscoring its robustness and optimization efficiency. Moreover, when compared to a PSO-based synchronization algorithm, the DE approach achieved a 20.29 % reduction in computational time, which underscores its computational efficiency and suitability for real-time applications.

The robustness of the control method is reinforced by an extensive sensitivity analysis encompassing 500 diverse demand scenarios. Key metrics include a minimum ITSE of 0.1937, a maximum ITSE of 0.362, an average ITSE of 0.2459, a standard deviation of 0.041, and a statistical mode of 0.2311. These statistics highlight consistent and reliable control performance across varying load conditions, reflecting the method's ability to maintain stability and dynamically adjust to abrupt changes. Further validation under MG fault conditions confirmed the method's resilience; frequency and voltage remained within defined thresholds, demonstrating the control's practical applicability in real-time dynamic environments and its ability to maintain system integrity during contingencies.

Finally, the real-time feasibility of the DE-based synchronization was experimentally validated via Hardware-in-the-Loop testing using OPAL-RT4512 and dSPACE MicroLabBox platforms. Experimental data under a 50 μs sampling time closely matched simulation results, confirming the control's precision and operational viability in compliance with IEEE Std. 1547–2018.

Building on the methodologies and findings presented in this study, some promising research directions emerge to further advance synchronization control in MGs. A key area for future exploration is enhancing the control framework to better handle practical communication challenges. These include variable delays, data loss, and limited bandwidth, which are inherent in distributed MG environments. Incorporating adaptive or robust control strategies capable of preserving synchronization under such conditions could significantly enhance system resilience and performance.

On the optimization front, future work could focus on developing more computationally efficient algorithms or hybrid approaches. These would aim to maintain high-quality solutions while reducing execution time, thereby improving the feasibility of real-time implementation and supporting scalability to larger and more complex MG networks. Techniques for adaptive parameter tuning may also be considered to dynamically adjust algorithm behavior based on changing system conditions.

Moreover, extending the proposed approach to heterogeneous MGs with diverse generation technologies and demand profiles would broaden its practical applicability. The integration of forecasting tools and learning-based strategies could further strengthen control performance by enabling more anticipatory and data-driven decision-making processes.

CRediT authorship contribution statement

Pablo Horrillo-Quintero: Conceptualization, Data curation, Formal analysis, Investigation, Methodology, Resources, Software, Validation, Visualization, Writing – original draft. **Pablo García-Triviño:** Conceptualization, Investigation, Methodology, Resources, Software, Validation, Visualization, Writing – original draft. **David Carrasco-González:** Conceptualization, Formal analysis, Investigation, Methodology, Writing – original draft. **Luis M. Fernández-Ramírez:** Conceptualization, Funding acquisition, Investigation, Methodology, Project administration, Supervision, Validation, Visualization, Writing – review & editing.

Declaration of competing interest

The authors declare that they have no known competing financial interests or personal relationships that could have appeared to influence the work reported in this paper.

Acknowledgments

This work was partially supported by Ministerio de Ciencia e Innovación, Agencia Estatal de Investigación, FEDER, UE (Grant PID2021-123633OB-C32 supported by MCIN/AEI/10.13039/501100011033/FEDER, UE).

Data availability

Data will be made available on request.

References

Jin, H., Nengroo, S. H., Jin, J., Har, D., & Lee, S. (2024). P2P power trading based on reinforcement learning for nanogrid clusters. *Expert Systems with Applications, 255*. https://doi.org/10.1016/j.eswa.2024.124759

Gabbar, H. A., & Abdelsalam, A. A. (2014). Microgrid energy management in grid-connected and islanding modes based on SVC. *Energy Convers Manag, 86*, 964–972. https://doi.org/10.1016/j.enconman.2014.06.070

Tang, C., Qin, Y., Wu, F., & Tang, Z. M. F. R. L. (2025). A model-free reinforcement learning model for energy storage in microgrid systems. *Expert Systems with Applications.* , Article 127602. https://doi.org/10.1016/j.eswa.2025.127602

Liu, C. C., Tse, C. K., & Yang, J. (2024). Nonlinear Behavior and Transient Stability of Grid-following Converters using Direct Power Control under Weak Grid. *IEEE Trans Sustain Energy*. https://doi.org/10.1109/TSTE.2024.3413343

Hmad, J., Houari, A., Bouzid, A. E. M., Saim, A., & Trabelsi, H. (2023). A Review on Mode transition strategies between Grid-Connected and Standalone operation of Voltage Source Inverters-based Microgrids. *Energies (Basel), 16*. https://doi.org/10.3390/en16135062

Yi, X., Peng, Y., Zhou, Q., Huang, W., Xu, L., Shen, Z. J., et al. (2022). Transient Synchronization Stability Analysis and Enhancement of Paralleled Converters considering different Current Injection strategies. *IEEE Trans Sustain Energy, 13*, 1957–1968. https://doi.org/10.1109/TSTE.2022.3176919

Koohi-Kamali, S., & Rahim, N. A. (2016). Coordinated control of smart microgrid during and after islanding operation to prevent under frequency load shedding using energy storage system. *Energy Convers Manag, 127*, 623–646. https://doi.org/10.1016/j.enconman.2016.09.052

D'Silva, S., Shadmand, M., Bayhan, S., & Abu-Rub, H. (2020). Towards grid of microgrids: Seamless transition between grid-connected and islanded modes of operation. *IEEE Open Journal of the Industrial Electronics Society, 1*, 66–81. https://doi.org/10.1109/OJIES.2020.2988618

Rezaei, N., & Kalantar, M. (2015). Smart microgrid hierarchical frequency control ancillary service provision based on virtual inertia concept: An integrated demand response and droop controlled distributed generation framework. *Energy Convers Manag, 92*, 287–301. https://doi.org/10.1016/j.enconman.2014.12.049

A. Ghosh F. Zare Control of Power Electronic Converters with Microgrid applications 2023 Wiley 10.1002/9781119815464.

Ganjian-Aboukheili, M., Shahabi, M., Shafiee, Q., & Guerrero, J. M. (2020). Seamless transition of Microgrids operation from Grid-Connected to Islanded Mode. *IEEE Transactions on Smart Grid, 11*, 2106–2114. https://doi.org/10.1109/TSG.2019.2947651

Hennane, Y., Berdai, A., Pierfederici, S., Meibody-Tabar, F., & Martin, J. P. (2022). Novel non-linear control for synchronization and power sharing in islanded and grid-connected mesh microgrids. *Electric Power Systems Research, 208*. https://doi.org/10.1016/j.epsr.2022.107869

Shahab, M., & Wang, S. (2021). Seamless transition strategy for Micro-grid Inverter based on improved Droop Control Strategy. In *2021 4th International Conference on Energy, Electrical and Power Engineering, CEEPE 2021, Institute of Electrical and Electronics Engineers Inc* (pp. 782–787). https://doi.org/10.1109/CEEPE51765.2021.9475781

Cao, W., Han, M., Meng, X., Xie, W., Khan, Z. W., Guerrero, J. M., et al. (2023). Reverse Droop Control-based Smooth transfer strategy for Interface Converters in Hybrid AC/DC distribution Networks. *CSEE Journal of Power and Energy Systems, 9*, 122–134. https://doi.org/10.17775/CSEEJPES.2020.02070

Huaman, J. F., Dos Santos, L. E., Ugaz Pena, J. C., Pomilio, J. A., & Dotta, D. (2024). Seamless Transitions between Grid-Tied and Islanded operation in a Brazilian Microgrid. *IEEE Power and Energy Society General Meeting, IEEE Computer Society*. https://doi.org/10.1109/PESGM51994.2024.10688385

Liu H, Qin X, Ding B, Fan Y. Grid-connected/Grid-islanded Smooth Switching Control of VSG Converter Based on Pre-synchronization. Proceedings - 2024 3rd Asian Conference on Frontiers of Power and Energy, ACFPE 2024, Institute of Electrical and Electronics Engineers Inc.; 2024, p. 43–8. doi: 10.1109/ACFPE63443.2024.10800929.

Gong, R., Qin, Y., Liu, T., Xu, J., & Wei, Z. (2024). Microgrid Pre-Synchronization Scheme for Suppressing Voltage Fluctuations and avoiding Frequency Out-of-Limits. *Electronics (Switzerland), 13*. https://doi.org/10.3390/electronics13020428

Awal, M. A., Yu, H., Tu, H., Lukic, S. M., & Husain, I. (2020). Hierarchical control for virtual oscillator based grid-connected and islanded microgrids. *IEEE Transactions on Power Electronics, 35*, 988–1001. https://doi.org/10.1109/TPEL.2019.2912152

Talapur, G. G., Suryawanshi, H. M., Xu, L., & Shitole, A. B. (2018). A Reliable Microgrid with Seamless transition between Grid Connected and Islanded Mode for Residential Community with Enhanced Power Quality. *IEEE Transactions on Industry Applications, 54*, 5246–5255. https://doi.org/10.1109/TIA.2018.2808482

Khan, M. Y. A., Liu, H., Zhang, R., Guo, Q., Cai, H., & Huang, L. (2023). A unified distributed hierarchal control of a microgrid operating in islanded and grid connected modes. *IET Renewable Power Generation, 17*, 2489–2511. https://doi.org/10.1049/rpg2.12716

Li, Z., Zhang, J., Cheng, Z., Si, J., Wang, Y., & Wang, X. (2024). Distributed cooperative grid synchronization strategy for multiple parallel grid-supporting inverters in AC microgrid. *International Journal of Electrical Power and Energy Systems, 155*. https://doi.org/10.1016/j.ijepes.2023.109624

Yadav, V., Singh, B., & Verma, A. (2024). Robust control for improving performance of grid-synchronized solar PV-BES-wind based microgrid. *Sustainable Energy Technologies and Assessments, 64*. https://doi.org/10.1016/j.seta.2024.103677

Buduma, P., Das, M. K., Naayagi, R. T., Mishra, S., & Panda, G. (2021). Seamless operation of Master-Slave Organized AC Microgrid with Robust Control and Islanding Detection. In *3rd International Conference on Energy, Power and Environment: Towards Clean Energy Technologies, ICEPE 2020, Institute of Electrical and Electronics Engineers Inc*. https://doi.org/10.1109/ICEPE50861.2021.9404425

Khan, M. Y. A., Liu, H., Shang, J., & Wang, J. (2023). Distributed hierarchal control strategy for multi-bus AC microgrid to achieve seamless synchronization. *Electric Power Systems Research, 214*. https://doi.org/10.1016/j.epsr.2022.108910

Hmad, J., Houari, A., Trabelsi, H., & Machmoum, M. (2019). Fuzzy logic approach for smooth transition between grid-connected and stand-alone modes of three-phase DG-inverter. *Electric Power Systems Research, 175*. https://doi.org/10.1016/j.epsr.2019.105892

Fachini, F., Bogodorova, T., Vanfretti, L., & Boersma, S. (2024). A microgrid control scheme for islanded operation and re-synchronization utilizing Model Predictive Control. *Sustainable Energy, Grids and Networks, 39*. https://doi.org/10.1016/j.segan.2024.101464

Meng, J., Zhang, Z., Zhang, G., Ye, T., Zhao, P., Wang, Y., et al. (2023). Adaptive model predictive control for grid-forming converters to achieve smooth transition from islanded to grid-connected mode. *IET Generation, Transmission and Distribution, 17*, 2833–2845. https://doi.org/10.1049/gtd2.12859

Li, X., Zhang, H., Shadmand, M. B., & Balog, R. S. (2017). Model Predictive Control of a Voltage-Source Inverter with Seamless transition between Islanded and Grid-Connected Operations. *IEEE Transactions on Industrial Electronics, 64*, 7906–7918. https://doi.org/10.1109/TIE.2017.2696459

Poonahela, I., Krama, A., Bayhan, S., Fesli, U., Shadmand, M. B., Abu-Rub, H., et al. (2023). Hierarchical Model-Predictive Droop Control for Voltage and Frequency Restoration in AC Microgrids. *IEEE Open Journal of the Industrial Electronics Society, 4*, 85–97. https://doi.org/10.1109/OJIES.2023.3240070

Xu, W., Wang, B., Liu, J., & Li, D. (2021). An improved droop control strategy for grid-connected inverter applied in grid voltage inter-harmonics and fundamental frequency fluctuation. *Electronics (Switzerland), 10*. https://doi.org/10.3390/electronics10151827

Naderi, M., Shafiee, Q., Blaabjerg, F., & Bevrani, H. (2023). Synchronization Stability of Interconnected Microgrids with fully Inverter-based distributed Energy Resources. *Journal of Modern Power Systems and Clean Energy, 11*, 1257–1268. https://doi.org/10.35833/MPCE.2022.000594

Ransom DL. Get in step with synchronization. IEEE Trans Ind Appl, vol. 50, Institute of Electrical and Electronics Engineers Inc.; 2014, p. 4210–5. doi: 10.1109/TIA.2014.2346698.

Std, I. E. E. E. (2018). 1547-2018 (Revision of IEEE Std 1547-2003) : IEEE Standard for Interconnection and Interoperability of distributed Energy Resources with Associated Electric Power Systems Interface. *IEEE*.

Alrajhi, H. (2024). A Novel Synchronization Method for Seamless Microgrid Transitions. *Arabian Journal for Science and Engineering, 49*, 6867–6881. https://doi.org/10.1007/s13369-023-08454-9

IEEE Texas Power and Energy Conference (TPEC) : Dat location: Memorial Student Center at Texas A & M University, 275 Joe Routt Blvd #2240 2020 College Station, TX, USA. IEEE.

Saxena, N. K., Gao, W. D., Kumar, A., Mekhilef, S., & Gupta, V. (2022). Frequency regulation for microgrid using genetic algorithm and particle swarm optimization tuned STATCOM. *International Journal of Circuit Theory and Applications, 50*, 3231–3250. https://doi.org/10.1002/cta.3319

Zulueta, A., Azurmendi, I., Rey, N., Zulueta, E., & Fernandez-Gamiz, U. (2022). Particle swarm optimization algorithm for dynamic synchronization of smart grid. *Energy Sources, Part A: Recovery, Utilization, and Environmental Effects, 44*(2), 3940–3959. https://doi.org/10.1080/15567036.2022.2069304

Hou, S., Desta Gebreyesus, G., & Fujimura, S. (2024). Day-ahead multi-modal demand side management in microgrid via two-stage improved ring-topology particle swarm optimization. *Expert Systems with Applications, 238*. https://doi.org/10.1016/j.eswa.2023.122135

Abhinav, S., Schizas, I. D., Ferrese, F., & Davoudi, A. (2017). Optimization-based AC Microgrid Synchronization. *IEEE Trans Industr Inform, 13*, 2339–2349. https://doi.org/10.1109/TII.2017.2702623

Mallipeddi R, Suganthan PN. Differential evolution algorithm with ensemble of parameters and mutation and crossover strategies. Lecture Notes in Computer Science (including subseries Lecture Notes in Artificial Intelligence and Lecture Notes in Bioinformatics), vol. 6466 LNCS, 2010, p. 71–8. doi: 10.1007/978-3-642-17563-3_9.

Gao, Y., & Liu, J. (2012). Multiobjective differential evolution algorithm with multiple trial vectors. *Abstract and Applied Analysis*. https://doi.org/10.1155/2012/172041

Al-butti, O. S., & Altinoz, O. T. (2023). Comparison between PSO-Based and fmincon-based Approaches of Optimal Power Flow for a Standard IEEE-30 bus. *System*, 209–219. https://doi.org/10.1007/978-3-031-30171-1_23

Pashaei, M., Rastegar, H., Zandrazavi, S. F., Kauhaniemi, K., & Laaksonen, H. (2024). Real-time hardware-in-the-loop approach for adaptive centralized protection schemes using clustering algorithms. *Expert Systems with Applications, 255*. https://doi.org/10.1016/j.eswa.2024.124707